Title:

Efferocytosis reprograms the tumour microenvironment and promotes pancreatic cancer liver metastasis

AUTHORS:

Yuliana Astuti[1], Meirion Raymant[1], Valeria Quaranta[1], Kim Clarke[2], Maidinaimu Abudula[1], Olivia Smith[1], Gaia Bellomo[1], Vatshala Chandran-Gorner[1], Craig Nourse[3], Christopher Halloran[1], Paula Ghaneh[1], Daniel Palmer[1], Robert P. Jones[1], Fiona Campbell[1], Jeffrey W. Pollard[4], Jennifer P. Morton[3,5], Ainhoa Mielgo[1], Michael C. Schmid[1*]

[1] Department of Molecular and Clinical Cancer Medicine, University of Liverpool, Ashton Street, Liverpool, L69 3GE, UK.

[2] Computational Biology Facility, University of Liverpool, Crown Street, Liverpool, L69 7ZB, UK.

[3] Cancer Research-UK Beatson Institute, Switchback Road, Glasgow, G61 1BD, UK.

[4] MRC Centre for Reproductive Health, University of Edinburgh, Little France Crescent, Edinburgh, EH16 4TJ, UK.

[5] School of Cancer Sciences, University of Glasgow, Switchback Road, Glasgow, G61 1BD, UK.

[*] to whom correspondence should be addressed mschmid@liv.ac.uk

Key words: pancreatic cancer, metastasis, tumour microenvironment, macrophages, efferocytosis, lysosomal function, immune-suppression

Running title: Efferocytosis promotes pancreatic cancer metastasis

ABSTRACT:

Pancreatic cancer (PDAC) is a highly metastatic disease and macrophages support liver metastases. Efferocytosis, or engulfment of apoptotic cells by macrophages, is an essential process in tissue homoeostasis and wound healing, but its role in metastasis is less well understood. Here, we found that the colonisation of the hepatic metastatic site is accompanied by low grade tissue injury and that efferocytosis-mediated clearance of parenchymal dead cells promotes macrophage reprogramming and liver metastasis. Mechanistically, progranulin expression in macrophages is necessary for efficient efferocytosis by controlling lysosomal acidification via cystic fibrosis transmembrane conductance regulator (CFTR) and the degradation of lysosomal cargo, resulting in LXRα/RXRα-mediated macrophage conversion and upregulation of arginase 1. Pharmacological blockade of efferocytosis or macrophage-specific genetic depletion of progranulin impairs macrophage conversion, improves $CD8^+$ T cell functions, and reduces liver metastasis. Our findings reveal how hard-wired functions of macrophages in tissue repair contribute to liver metastasis and identify potential targets for prevention of PDAC liver metastasis.

INTRODUCTION:

Pancreatic ductal adenocarcinoma (PDAC) is a highly metastatic disease with a 5-year survival rate of less than 7%[1]. Metastatic spread is an early event in disease progression, commonly occurs to the liver and is the primary cause of death for PDAC patients[2]. By the time PDAC is diagnosed, the majority (~80%) have non-resectable metastatic cancer[3–5]. In addition, around 70% of the patients whose primary tumour is removed relapse with hepatic metastasis within 2 years of surgery[3–5]. A better understanding of the mechanisms underlying the metastatic process in pancreatic cancer is therefore critical to improve outcomes for these patients.

The effective clearance of dying cells is a fundamental process in homeostasis, tissue repair, and disease[6]. The engulfment of dead cells by phagocytes, a process known as efferocytosis,

is performed by macrophages and to a lesser extent by other cells[7]. Macrophages are critical immune cells and are highly plastic. Liver metastasis is accompanied by the accumulation of a high number of macrophages[8,9]. Depending on their activation state, they can acquire tumour repressive or tumour supportive functions[10,11]. Unfortunately, in progressing tumours, including metastatic tumours in PDAC, macrophages often display an immunosuppressive phenotype, promoting tumour growth and limiting the impact of immunotherapy[12–14].

Emerging studies indicate that tumour associated macrophages are highly diverse and can co-exist within the same tumour as immunostimulatory and immunosuppressive subtypes[15]. Thus, therapeutically enhancing the presence of immunostimulatory macrophages by either a tailored stimulation or by impairing their conversion towards an immunosuppressive subtype holds great promise to improve current treatment options for cancer patients.

RESULTS

Identification of diverse metastasis-associated macrophage populations in metastatic livers by combining single cell analysis with spatial in-situ labelling strategy

To better understand the immunological status of advanced metastatic lesions in PDAC patients, we first collected fresh liver biopsies from treatment-naïve metastatic PDAC patients and performed bulk RNA sequencing. We found that metastatic lesions are immune silenced, with an enrichment of macrophages and neutrophils, and low signature scores for T cells, B cells, and NK cells (Fig. 1a). Using immunofluorescence tissue staining of advanced metastatic PDAC lesions we observed that the peripheral regions of metastatic lesions are rich in macrophages ($CD68^+$) and T cells ($CD8^+$), although these are largely Granzyme B negative (Fig. 1b,c and Extended Data Fig. 1a,b). In contrast, while macrophages were also abundant in the metastatic core region, $CD8^+$ T cells were virtually absent (Fig. 1b,d and Extended Data Fig. 1a,b). Together, these findings show that the metastatic tumour microenvironment in PDAC is immunosuppressive, characterised by high numbers of metastasis associated macrophages (MAMs) and poor $CD8^+$ T cell infiltration.

To characterise MAM heterogeneity in pancreatic cancer liver metastasis *in vivo*, we next induced liver metastasis by intra-portal injection of KPC-derived cells, isolated from the genetically engineered mouse model of PDAC (*Kras*^{G12D}; *Trp53*^{R172H}; *Pdx1-Cre*), in orthotopic PDAC tumour bearing mice. We then performed single cell RNA sequencing on MAMs isolated by flow cytometry using an APC-conjugated pan-macrophage marker F4/80 ($CD45^+F4/80^{APC+}$) (Extended Data Fig. 1c). We collected MAMs from early metastatic (day 5) and advanced metastatic lesions (day 10). To resolve the spatial distribution of MAMs in advanced metastatic lesions, we developed an *in-situ* antibody labelling approach where tumour bearing livers were perfused with FITC-conjugated F4/80 ($F4/80^{FITC}$) antibody solution. Since established metastatic liver tumours in PDAC are highly fibrotic and poorly vascularised[16], the *in-situ* perfusion of metastasis bearing mice mainly stains macrophages in the peripheral area of metastatic lesions ($F4/80^{FITC+}$), while intra-metastatic macrophages remain unstained ($F4/80^{FITC–}$) (Extended Data Fig. 1d-g). We thus defined unstained

macrophages as metastasis-proximal macrophages (pMAMs) and stained macrophages as metastasis-distal macrophages (dMAMs).

After application of quality control and exclusion of cells lacking expression of pan-macrophage genes *Adgre1* or *Cd68*, macrophages from the following four groups were subsequently analysed: healthy livers (2428 cells), early metastasis (2007 cells), advanced metastasis proximal (1953 cells), and advanced metastasis distal (2783 cells). Seurat-based clustering and dimensionality reduction using Uniform Manifold Approximation and Projection (UMAP) revealed 10 distinct populations (Fig. 1e). Macrophages in the liver can originate from both embryonic macrophages (Kupffer cells, KC) and monocytes recruited from the bone marrow[17]. Clusters 0, 1, 4, 5, 6, 8, and 9 were identified as KC subsets by their high expression of previously reported KC markers such as *Clec4f, Vsig4,* and *Timd4*[18] (Fig. 1f,g and Extended Data Fig. 1h). In parallel, clusters 2, 3, and 7 were identified as monocyte-derived macrophage (MoM) subsets based on their expression of *Ccr2*[19] (Fig. 1f,g and Extended Data Fig. 1h).

In tumour-free livers, we found that the liver macrophage population is largely dominated by KC subsets, especially cluster 0, while MoM subsets were only minimally present (Fig. 1h), thereby confirming previous reports[18,20]. In the livers with metastatic lesions, cluster 1, 4, 6, and 8 of the KC subsets and all 3 MoM clusters were expanded compared to tumour-free livers and were therefore identified as metastasis induced macrophages (Fig. 1h,i and Extended Data Fig. 1i). We next carried out a characterisation of the identified macrophage clusters based on their differentially expressed gene (DEG) signatures. Cluster 0, which dominated (75%) the macrophage population in naïve liver, was characterised by high expression of previously reported KC genes[18], including *Vsig4*, *C6*, *Folr2*, *Clec4f*, *Apoc1*, and *Timd4* (Fig. 1j and Supplementary Table 1), which were also found to be highly expressed in the KC clusters: 1, 5, 6, 8, and 9. In addition to these pan KC markers, cluster 5 (10% of naïve liver macrophages) highly expressed antigen processing and presentation genes (*H2-Eb1*, *H2-Ab1*, *H2-T23*, and *H2-D1*) (Fig. 1j and Supplementary Table 6). Cluster 9 (2% of naïve liver macrophages) showed endothelial-like characteristics by their high expressions of *Clec4g, Kdr*, *Ptprb*, and *Egfl7* (Fig. 1j and Supplementary Table 10).

The two major MAM clusters derived from KCs, cluster 1 and 4, showed an inflammatory signature with high expression of pro-inflammatory cytokines, such as *Il6*, *Il1a*, *Il1b*, and *Il18* and NF-kβ and MAPK signalling pathway genes (*Nfkbiz*, *Fosb*, *Trim25*, *Nfkbia*, *Map3k8*) (Fig. 1j,k and Supplementary Table 2 and 5). This was accompanied by expression of the inflammation repressors *Egr1* and *Il10*, suggesting a negative feedback mechanism (Fig. 1j,k and Supplementary Table 2 and 5). While cluster 1 shared most of its DEGs with cluster 4, the latter was uniquely characterised by expression of genes such as the leptin receptor *Lepr*, which, together with high expressions of *Scd1*, *Tnf*, *Il1b*, and *Il6*, suggests a pro-fibrogenic phenotype[21,22]. The remaining KC-MAM subsets were determined to be proliferating macrophages due to their high expression of cell cycle genes (*Stmn1*, *Cenpa*, *Mki67*) in cluster 6 and DNA replication genes (*Mcm5*, *Mcm6*, *Topbp1*) in cluster 8 (Fig. 1j and Supplementary Table 7 and 9).

Within monocyte-derived MAM subsets, cluster 2 exhibited an antigen presentation and processing (AP) gene signatures, demonstrated by high expression of *H2-Eb1*, *H2-Ab1*, and *Cd74* (Fig. 1j,k and Supplementary Table 3). Conversely, cluster 3 showed enrichment of *Chil3*, *Mrc1*, and *Arg1*, suggesting an M2-like/immunosuppressive phenotype (Fig. 1j,k and Supplementary Table 4). The minor MoM population, cluster 7, displayed similar expression of *Chil3* and *Arg1* and high expression of cell cycle genes (*Stmn1*, *Cenpa*, *Mki67*), suggesting that it is a proliferating subset of cluster 3 (Fig. 1j and Supplementary Table 8).

To assess the relevance of this mouse data, we next explored whether the identified MAM signatures were present in our human PDAC liver metastasis RNA sequencing data. Indeed, we found that all four MAM signatures (clusters 1 and 4 KC, clusters 2 and 3 MoMs) were detectable in human data (Extended Data Fig. 1j). In agreement with our scRNAseq analysis that revealed cluster 3 MoMs to be the most abundant subset in core areas of advanced metastasis, we found the highest signature score for this cluster in all liver biopsies taken from cores of advanced metastatic tumours of PDAC patients (Fig. 1l).

Together, these data suggest that PDAC metastasis increases macrophage heterogeneity in both recruited MoM and tissue-resident KCs and that immunosuppressive and immunostimulatory macrophage subpopulations co-exist.

CD74$^{neg/low}$ MoMs display potent immunosuppressive functions at an early metastatic stage

We next analysed the spatial distribution of the identified MAM clusters based on our *in-situ* labelling approach. As expected, pMAM and dMAM subsets from advanced liver metastasis displayed minimal overlap further confirming the specificity of our labelling approach (Fig. 2a). Notably, we found that metastasis infiltrating pMAMs originate from monocytes while dMAMs are mainly comprised of tissue resident KC, consistent with a previous reports[23] (Fig. 2b). In agreement with these findings, tissue section analyses of advanced metastatic lesions derived from PDAC patients (Fig. 2c,d), the autochthonous KPC mouse model (Extended Data Fig. 2a,b), and the experimental metastasis mouse model (Extended Data Fig. 2c,d), all confirmed that metastatic tumours were highly infiltrated by macrophages, but that macrophages located in peripheral areas of metastatic lesions stained positive for the KC marker VSIG4, while macrophages within the core were VSIG4-negative. These data suggest that recruited MoMs infiltrate the metastatic lesions, while MAMs distal to metastatic lesions originate from tissue resident KCs.

As we observed that pMAMs in advanced metastasis are predominantly derived from monocytes, we focused our subsequent analyses on the 3 MoM subsets. We performed an additional clustering and UMAP analysis of MoM populations (cluster 2, 3, and 7) and found 6 further distinct MoM clusters (Fig. 2e). Within the AP positive-associated subset (cluster 2 in original UMAP), we found three new clusters (B, C, and F). Interestingly, AP signature was found to be enriched in cluster B and F (AP^{high}), but not in cluster C (AP$^{-/low}$) (Fig. 2f). Furthermore, cluster C was associated with phagocytosis/apoptotic cell clearance signatures (*Cd300a*, *Cd36*, *Scarb1*, *Anxa2*, *Gpnmb*) and enriched in lysosomal genes (*Lipa*, *Ctsb*, *Ctsd*, *Psap*, *Grn*) (Fig. 2f and Extended Data Fig. 2e), suggesting that cluster C is a population of

efferocytic macrophages. Two clusters (cluster A and E) were derived from the M2-like/immunosuppressive subset (cluster 3 in original UMAP) (Fig. 2f and Extended Data Fig. 2e). Both clusters lacked expressions of AP genes (AP^{-}) and showed higher expressions of M2 marker genes *Chil3* and *Mrc1*, however cluster E also displayed an inflammatory signature, as shown by expressions of Nf-κB and TNFα signalling pathways-related genes such as *Il6, Tnf, and Il1a* (Fig. 2f and Extended Data Fig. 2e). The remaining subset, cluster D, displayed enrichment of cell cycle genes and similar profile to cluster A, suggesting that cluster D is a proliferating subset of cluster A (Fig. 2f and Extended Data Fig. 2e).

In early metastasis, the MoM population was dominated by cluster C with a minor contribution from the AP^{high} associated subsets, clusters B and F, while the advanced metastatic lesions were dominated by cluster B and the M2-like subset cluster A, followed by clusters E and D (Fig. 2h,i). Pseudotime analysis revealed a phenotype trajectory that starts with cluster F, followed by cluster C and cluster B, and final differentiation into cluster A/D or E during metastatic progression (Extended Data Fig 2f). In pre-metastatic liver isolated from mice with orthotopically-implanted tumour, we detected AP^{hi} and cluster C/E-like MoM populations (Extended Data Fig. 2g-k), suggesting that cancer-educated MoM population in the liver already appear during pre-metastatic niche formation in tumour-bearing mice. Consistently, cluster A-like population dominated MoM populations in livers with advanced spontaneous metastasis isolated from mice orthotopically implanted with KPC tumour organoids (Extended Data Fig. 2g-k).

Given that the major MoM populations (clusters A, B, and C) are distinguishable based on AP and M2 marker gene expression, we next performed immunostaining of AP protein CD74 and M2-marker *Chil3*-encoded YM-1 on early and advanced metastatic tissues isolated from post intrasplenic KPC cell implantation livers at d5 and d14, which had comparable tumour burden as d10 post intraportal implantation (Extended Data Fig. 2l). As expected, $CD74^{-/low}$ $YM\text{-}1^{-}$ MoMs (cluster C) are most abundant in early metastatic lesions, while $CD74^{-/low}$ $YM\text{-}1^{+}$ MoMs (cluster A) represented the most frequent MoM subset in advanced metastatic lesions (Fig. 2i-k).

To characterise the functional phenotype of AP^{high} versus $AP^{-/low}$ MoMs, we next isolated $CD74^{hi}$ and $CD74^{-/low}$ MoMs ($F4/80^{+}TIM4^{-}$) from early and advanced metastatic tumours using FACS and co-cultured them with activated $CD8^{+}$ T cells. In the early and advanced metastatic lesions setting, $CD74^{-/low}$ MoMs were more potent in inhibiting $CD8^{+}$ T cell functions compared to $CD74^{hi}$ MoMs (Fig. 2l). We observed lower immunosuppressive activity in late $CD74^{-/low}$ MoMs compared to early $CD74^{-/low}$ MoM, which may be attributed to the inflammatory subset of MoMs (cluster E) present in late $CD74^{-/low}$ MoMs (Fig. 2g) that express T-cell stimulating factors such as *Il1a* and *Tnf* [24,25]. Taken together, out data suggest that the acquisition of an immunosuppressive phenotype in MoMs occurs early during metastasis formation and is associated with the loss of CD74 expression and the presence of an efferocytosis gene signature.

Tissue resident cell death induces efferocytosis-mediated macrophage conversion from an immunostimulatory to an immunosuppressive phenotype

Macrophages are instrumental to tissue repair by the clearance of dead cells through efferocytosis. We therefore reasoned that the observed pathway signatures in MoMs might be induced by metastasis related liver injury. To test this, we next examined the presence and extent of metastasis related injury in the livers derived from i) the autochthonous KPC model, ii) the experimental intrasplenic metastasis model, and iii) after daily intravenous administration of pancreatic tumour conditioned medium (TCM) into healthy mice. Indeed, patches of hepatic necroses were detected in liver tissues of the autochthonous KPC model, post orthotopic implantation of KPC cells, and at early stages of the experimental intrasplenic metastasis model, even in the absence of microscopic detectable metastatic lesions in the liver (Fig. 3a and Extended Data Fig.3a). Moreover, daily administration of pancreatic TCM was sufficient to induce hepatic necroses (Fig. 3b,c). Thus, PDAC liver metastasis is accompanied by death of tissue resident cells which occurs during initial events of metastatic spreading or even in response to tumour-derived factors. To confirm the presence of

efferocytic MoMs, we performed transplantation of wildtype bone marrow cells into tdTomato-expressing (tdT^+) mice resulting in chimeric mice that have ubiquitous expression of red tdT, including in hepatocytes and KCs, while MoMs remained unlabelled (Fig. 3d). Following induction of liver metastasis, the accumulation of tdT^- MoMs was observed in the necrotic areas, some of which contain tdT^+ debris in their cytoplasm (Fig. 3e). Taken together, our data show that at early stage of PDAC metastasis an efferocytotic MoM subpopulation emerges to resolve metastasis-associated tissue injuries in the liver.

To identify the mediator of the immunosuppressive activity observed in the early MoM subset, we next examined expression of immunosuppressive genes in the MoM population in our scRNAseq data. We found expression of the T cell inhibitory gene *Arg1* in cluster C MoMs, which may be responsible for the immunosuppressive activity we observed in early $CD74^{-/low}$ MoMs (Extended Data Fig. 3b). Furthermore, arginase 1 has been previously linked to efferocytosis [26,27]. Consistent with the presence of liver injury prior to metastatic engraftment, high expression of *Arg1* was also found in MoM populations isolated from pre-metastatic livers of mice with orthotopically-implanted tumour (Extended Data Fig. 3c). *In vitro* cell culture assays using primary mouse macrophages confirmed that efferocytosis is sufficient to induce the upregulation of *Arg1*/arginase 1 on gene and protein level, respectively (Fig. 3g-h and Extended Data Fig. 3f). Similar results were observed in primary human macrophages (Extended Data Fig. 3g).

To functionally test the biological relevance of arginase 1, we next stimulated $CD8^+$ T cells and co-cultured them with $CD74^{neg/low}$ early MoMs (Fig. 3i,j) or efferocytic macrophages (Fig. 3k,l) in the presence of an arginase 1 inhibitor, CB1158. Similar to early MoMs, efferocytic macrophages showed markedly increased immunosuppressive activity (Fig. 3i-l) and treatment with arginase 1 inhibitor CB1158 (ARGi) abrogated this effect, suggesting that arginase 1 is responsible for the T cell-suppressing activity of efferocytic macrophages (Fig. 3i-l). Blockade of arginase 1 activity also reduced T cell inhibitory effect of $CD74^{neg/low}$ late MoMs, suggesting that arginase 1 mediates immunosuppressive effect of both early and late $CD74^{neg/low}$ MoMs (Extended Data Fig. 3h,i). Notably, we also observed increased apoptosis

of stimulated $CD8^+$ T cells when co-culture with efferocytic macrophages *in vitro* (Extended Data Fig. 3j). In summary, we found that PDAC liver metastasis is accompanied by liver damage and the presence of efferocytic MoMs and that efferocytosis promotes the conversion of macrophages towards an immunosuppressive phenotype.

Inhibition of efferocytosis prevents MoM conversion and PDAC metastasis

We next assessed the biological function of efferocytosis induced macrophage conversion in PDAC liver metastases. For this, we first pharmacologically blocked macrophage efferocytosis *in vitro* using UNC2250, a small molecule inhibitor of MerTK (MerTKi). As expected, *in vitro*, the presence of MerTKi reduced efferocytosis in macrophages co-cultured with apoptotic thymocytes (Fig 4a,b) and ablated the induction of *Arg1* expression in macrophages (Fig. 4c and Extended Data Fig. 4a). Furthermore, MerTK inhibition reduced the T cell suppressing activity of efferocytic macrophages (Fig. 4d and Extended Data Fig. 4b).

To test the impact of efferocytosis on macrophage conversion *in vivo*, we next induced liver metastasis by intrasplenic implantation of KPC cells followed by treatment of the animals with MerTKi for 7 consecutive days (Fig. 4e). Hepatic necrotic areas were markedly increased in early metastatic lesions (d5) in livers derived from mice treated with MerTKi, suggesting a delay in clearance of apoptotic parenchymal cells due to impaired efferocytosis (Extended Data Fig. 4c,d). MerTKi administration did not affect early metastatic tumour burden however a significant reduction was found at advanced stage (Fig. 4f,g).

While cancer cells have been reported to express MerTK previously[28–30], we found that only a low percentage of the KPC-derived cell line FC1199 express this receptor (Extended Fig. 5e), suggesting that the MerTKi effect is not direct on cancer cell function. In contrast, MerTK expression was present in the majority of macrophages (Extended Data Fig. 4e). Gene expression analysis of isolated MoMs confirmed a significant reduction in *Arg1* expression in early metastatic lesions when efferocytosis is impaired (Fig. 4h). While abundance of MoMs

was not affected, MerTKi treatment caused a decrease in CD74^{-}YM-1^{-} and increase in CD74^{+}YM-1^{-} MoMs (Extended Data Fig. 4f-h).

STING/type I interferon pathway activation has previously been shown to occur following MerTK inhibition ([31]). We observed an increased *Ifnb1* among early MoMs, however this was not affected by MerTK inhibition (Extended Data Fig. 4i). Moreover, while MerTKi ablated the immunosuppressive activities of efferocytic macrophages, additional pharmacological blockade of STING did not show any effect, suggesting a dispensable role of the STING/type I interferon pathways in this setting (Extended Data Fig. 4j).

In agreement with the increased presence of less immunosuppressive macrophages in early metastatic lesions of MerTKi-treated mice, we found a significant increase of infiltrating CD8^{+} T cells (Fig. 4i,j) and among these, a significantly higher proportion of cytotoxic GzmB^{+} CD8^{+} T cells (Fig. 4i,k) and activated CD69^{+} CD8^{+} T cells (Extended Data Fig. 4k). As expected, depletion of CD8^{+} T cells ablated the anti-metastatic effect of MerTK treatment (Fig. 4l,m) suggesting that MerTKi acts through increasing cytotoxic T cell functions.

Interestingly, even in advanced metastatic tumours (d14), MerTKi treatment reduced expression of *Arg1* in MoMs (Extended Data Fig. 4l) without affecting the abundance of MoMs (Extended Data Fig. 4m,n). Furthermore, MerTKi-treated lesions contained fewer YM-1^{+} macrophages (Extended Data Fig. 4m,o), confirming that inhibition of efferocytosis in early metastasis impairs the phenotypic conversion of MoMs during metastatic progression *in vivo*. Similar reduction in metastatic tumour burden was also found with MerTK inhibition in spontaneous liver metastasis model (Fig. 4n,o) while primary tumours remained unaffected (Extended Data Fig. 4p). MerTK expression was also found to be absent in the KPC-derived organoid used in this model (Extended Data Fig. 4q). Expectedly, *Arg1* expression in MoMs was reduced with MerTKi treatment (Fig. 4p).

Since metastasis-associated liver injury induced a pro-tumourigenic MAM phenotype we next questioned whether pre-existing non-cancerous liver injury is sufficient to increase the presence of pro-tumourigenic MAMs and thereby makes livers more permissive for metastasis. To test this, we induced acute liver injury using a single dose of paracetamol (N-

acetyl-para-aminophenol or APAP) and two days later animals were challenged for liver metastasis by intrasplenic implantation of pancreatic cancer cells (Extended Data Fig. 5a). In agreement with previous studies[32,33], APAP induced hepatic necroses 24h after administration (Extended Data Fig. 5b). While APAP pre-treatment showed marginal effect on early metastatic outgrowth (Extended Data Fig. 5c), it resulted in significant increased tumour burden at advanced stage compared to vehicle pre-treatment (Extended Data Fig. 5d). In early metastatic lesions APAP pre-treatment did not affect $CD74^{+}YM\text{-}1^{-}$ MoMs (Extended Data Fig. 5e-g). Interestingly, APAP pre-treatment reduced the proportion of $CD74^{-}YM\text{-}1^{-}$ MoMs and increased $CD74^{-}YM\text{-}1^{+}$ MoMs (Extended Data Fig. 5e-g), indicating an accelerated MoM conversion into the late-stage M2-like phenotype. As expected, expression of *Arg1* in MoMs was reduced with APAP-pretreated compared to vehicle-treated animals (Extended Data Fig. 5h) while $CD8^{+}$ T cell infiltration (Extended Data Fig. 5i,j) and their cytotoxicity/activation state (Extended Data Fig. 5i,k,l) were significantly reduced. In advanced metastatic lesions of APAP-pre-treated mice, a sustained significant elevated *Arg1* expression (Extended Data Fig. 5m) was observed while MoM numbers only marginally increased (Extended Data Fig. 5n,o). Furthermore, increased proportion of $YM\text{-}1^{+}$ macrophages was found compared to vehicle control-derived livers (Extended Data Fig. 5p).

Taken together, our findings demonstrate that an efferocytosis-induced macrophage switch promotes PDAC liver metastasis and that this process can be blocked by inhibiting MerTK.

Depletion of progranulin prevents macrophage conversion and reduces PDAC liver metastasis

Given that blocking the clearance of necrotic cells leads to increased tissue damage, we reasoned that interfering with post-engulfment stages of efferocytosis may represent a better tolerated treatment strategy to suppress macrophage polarisation during PDAC liver metastasis. To identify a suitable macrophage specific target, we next filtered the upregulated genes in early cluster 2 MoM from our scRNAseq analysis for GO term “lysosome” and found that progranulin (*Grn*) was among the upregulated lysosomal genes (Extended Data Fig. 6a).

Progranulin is a precursor protein that is either secreted or transferred from the endoplasmic reticulum to the lysosomal compartment, where proteolytically cleaved smaller peptides of progranulin, called granulins, are thought to be critical for lysosome function in macrophages[34]. Previously, we have shown that macrophages are a major source of progranulin in PDAC liver metastasis[8] and depletion of progranulin has been associated with defective phagocytic activities in response to bacterial infections[35]. We thus hypothesised that progranulin might play a critical role in macrophage-mediated efferocytosis. In agreement with our hypothesis, we found that efferocytosis induces the expression of *Grn* in primary human and mouse macrophages (Extended Data Fig. 6b,c) and that progranulin specifically localises to the lysosomal compartment in primary mouse and human macrophages during efferocytosis (Fig. 5a-c).

We next assessed whether depletion of progranulin affects the efferocytosis-induced immunosuppressive macrophage polarisation *in vitro*. Indeed, efferocytosis-induced upregulation of *Arg1* expression (Fig. 5d,e) and suppression of $CD8^+$ T cell function were significantly reduced in progranulin-deficient (Grn KO) macrophages (Fig. 5f,g).

Next, we tested whether macrophage-specific depletion of progranulin affects MAM polarisation during PDAC liver metastasis *in vivo*. We intrasplenically implanted pancreatic cancer cells into conditional *Csf1r-MerCreMer*$^+$;*Grn*$^{fl/fl}$ mice (KO), in which administration of tamoxifen (Tam) induces depletion of progranulin specifically in macrophages and used *Csf1r-MerCreMer*$^-$;*Grn*$^{fl/fl}$ (WT) mice as control cohort (Fig. 5h and Extended Data Fig. 6d).

Macrophage-specific depletion of progranulin reduced metastatic tumour burden with significant changes found in the advanced stage (Fig. 5i,j). As expected, depletion of progranulin reduced expression of *Arg1* in isolated MoMs (Fig. 5k). Reduction in *Arg1* expression in MoMs was sustained in advanced metastasis (Extended Data Fig. 6e) along with reduction in YM-1^+ macrophage while macrophage abundance remained unaffected (Extended Data Fig. 6f-h). Lack of progranulin in macrophages led to a significant increase in total $CD8^+$ T cell numbers (Fig. 5l,m), in cytotoxic $GzmB^+$ $CD8^+$ T cells (Fig. 5l,n) and in activated $CD69^+$ $CD8^+$ T cells (Extended Data Fig. 6i) in early metastatic livers.

Depletion of progranulin in macrophage also resulted in reduced tumour burden in spontaneous liver metastasis model without significant change in the primary tumours (Fig. 5o,p and Extended Fig. 6pj). Consistently, *Arg1* expression in MoMs was also significantly diminished in this model (Fig. 5q).

Taken together, our data demonstrates that progranulin expression in macrophages is necessary for efferocytosis-induced conversion of MoMs into an immunosuppressive phenotype which then supports metastatic growth of pancreatic cancer cells in the liver.

Progranulin deficiency impairs lysosomal acidification and cargo degradation during efferocytosis

We next aimed to better understand the biological function of progranulin during efferocytosis and the resulting conversion of macrophages into an immunosuppressive phenotype. Therefore, we tested whether lack of progranulin affects efferocytosis of apoptotic cells and/or their proteolytic degradation in the lysosomes. Interestingly, progranulin-deficient macrophages (Grn KO) showed an increased accumulation of engulfed apoptotic cells (Fig. 6a,b), and increased retention of cargo in the lysosomal compartment over time (16h) (Fig. 6c,d). These data suggest that progranulin-deficient macrophages are able to uptake apoptotic cells, but that the processing of the cargo within the lysosome is impaired. Previously, progranulin has been reported to shuttle by its sortilin-binding domain to the lysosomal compartment[36] and to regulate lysosomal acidification during autophagy[37]. As efficient cargo destruction in the lysosome is regulated by acidification in the lumen into a low pH[38] we next measure lysosome acidification in wildtype and $GRN^{-/-}$ macrophages during efferocytosis. In wildtype (WT), but not in progranulin-deficient macrophages (Grn KO), the pH rapidly lowered and lysosomal acidification increased in phagolysosomes in response to efferocytosis (Fig. 6e,f). Importantly, in progranulin deficient cells (GRN KO), restoration of lysosomal acidification to WT level was achieved by exogenous expression of recombinant full length (FL) progranulin, but not by the expression of truncated progranulin lacking its

sortilin-binding domain (TR) or the expression of its sortilin-binding domain (SB) only (Extended Data Fig. 7a,b).

Upon proteolytic degradation of apoptotic cell cargo within the lysosome, resulting lipid products are sensed by nuclear sterol receptors such as LXRα, which has previously been reported to regulate *Arg1* expression[39]. Pharmacological inhibition of LXRα (LXRi; GSK-2033) ablated efferocytosis-induced *Arg1* expression in efferocytic WT macrophages but had no additional effect on Grn KO macrophages (Fig. 6g). Furthermore, LXRα target gene, *Abca1*[40], was upregulated in WT, but not granulin deficient, efferocytic macrophages (Fig. 6h), suggesting reduced LXRα activity in efferocytic Grn KO macrophages. In WT, but not in GRN KO macrophages, efferocytosis markedly increased the interaction of LXRα (encoded by *Nr1h3*) with its heterodimer partner RXRα[40] (Fig. 6i,j) while *Nr1h3* expression levels remained unchanged (Extended Data Fig. 7c). In agreement with increased LXRα activation in efferocytic WT macrophages, pharmacological blockade of LXRα reduced liver metastasis *in vivo* (Extended Data Fig. 7d,e).

As impairment of efferocytosis signalling has previously been linked to inducing an anti-tumour type I interferon immune response[41], we next wondered whether progranulin deficient macrophages show a similar response. We found that depletion of progranulin resulted in a significantly increased activation of type I interferon response as evidenced by elevated levels of nuclear IRF3 (Extended Data Fig. 7f) and upregulation of *Ifnb1* gene expression (Extended Data Fig. 7g). Taken together, our data suggest that impaired lysosomal function in progranulin-deficient macrophages pauses LXRα-mediated *Arg1* expression and instead leads to type I interferon activation in response to efferocytosis.

Progranulin supports efferocytosis and macrophage conversion by regulating lysosomal acidification via the cystic fibrosis transmembrane conductance regulator (CFTR)

We next aimed to identify the molecular mechanism by which progranulin regulates efferocytosis-induced lysosome acidification. Using the interactome database IntAct, we first analysed potential binding partners of progranulin that are localised within the lysosomal compartment, among which we identified cystic fibrosis transmembrane conductance regulator (CFTR). CFTR has previously been reported to regulate lysosome acidification in macrophages following phagocytosis of bacteria[42,43]. Proximity ligation assay of progranulin and CFTR confirmed their co-localisation in the cytoplasm of wildtype macrophages (Extended Data Fig. 8a). In agreement with this, the lack of progranulin depletes the presence of CFTR in lysosomes (Fig. 7a), while its expression levels remained unaffected (Extended Data Fig. 8b). Pharmacological inhibition of CFTR using CFTRinh172 (CFTRi) significantly impaired efferocytosis induced lysosomal acidification in macrophages (Extended Data Fig. 8c-d).

We next assessed whether inhibition of CFTR is sufficient to block efferocytosis-induced macrophage conversion *in vitro*. Indeed, CFTR inhibition significantly reduced *Arg1* expressions (Fig. 7b,c) and ablated the increased immunosuppressive activities of efferocytic WT macrophages, while CFTR inhibition did not show any effect on efferocytic progranulin-deficient macrophages (Fig. 7d,e).

To assess the impact of CFTR inhibition during PDAC liver metastasis, we performed intrasplenic implantation of KPC-derived cancer cells followed by treatment with CFTRi or vehicle control for 7 consecutive days (Fig. 7f). While CFTR inhibition caused a marginal effect on early metastatic tumour burden, a significant reduction was observed at advanced stage (Fig. 7g,h). In agreement with our *in vitro* finding, administration of CFTRi significantly reduced *Arg1* expression levels in MoMs (Fig. 7i), increased $CD8^+$ T cell infiltration (Fig. 7j,k), and their activation ($GzmB^+CD8^+$; $CD69^+CD8^+$ T cells) in early metastatic tumours (Fig. 7k,l and Extended Data Fig. 8e).

In advanced metastasis, CFTRi treated mice displayed sustained impaired *Arg1* expression in MoMs (Extended Data Fig. 8f) and inhibited macrophage conversion as shown by overall reduced numbers of YM-1^+ macrophages within metastatic lesions (Extended Data Fig. 8g-i).

Taken together, our findings show that progranulin regulates lysosomal acidification in macrophages via CFTR and that pharmacological blockade of lysosomal acidification with a CFTR inhibitor inhibits PDAC liver metastasis growth (Fig. 7m).

DISCUSSION

By developing a single-cell RNA sequencing and *in vivo* cell labelling approach, we reveal the spatial and temporal heterogeneity of macrophages in PDAC liver metastases. We confirm that macrophage tissue origin plays a key role in determining the localisation and function of these cells in metastatic liver tumours. While both recruited MoMs (TIM4^{-}/VSIG4^{-}) and tissue resident KCs (TIM4^{+}/VSIG4^{+}) expand during metastatic disease progression, MoMs are located within metastatic tumour lesions while KCs are mostly found at the margin areas. Our finding is consistent with recent studies that show enrichment of resident macrophages at the adjacent tissue[44–46]. Furthermore, we identify phenotypic changes within the KCs and MoMs during metastatic expansion. Induced by the colonisation of the liver by cancer cells, KCs display an inflammatory phenotype that is maintained throughout metastatic progression (cluster 1 and 4). However, at later stages of metastasis a subset of KCs acquires a pro-fibrotic signature (cluster 4), suggesting that this subset may contribute to hepatic stellate cell/fibroblast activation in advanced lesions and thereby help sustain the desmoplastic stroma in PDAC liver metastasis. In agreement with these findings, a pro-fibrotic phenotype of resident macrophages has recently been reported in primary PDAC and other cancer types[47]. Thus, tissue resident macrophages are undoubtedly also critical regulators of cancer metastases and our observed changes in KC clusters in response to metastatic tumours will hopefully inspire future studies to dissect the biological functions of tissue resident macrophages in PDAC liver metastasis. Within MoM subset, immunostimulatory and immunosuppressive phenotypes co-exist in early and advanced metastatic lesions. Strikingly, a phenotypic conversion towards an immunosuppressive subtype also occurs in both early and advanced stages of metastasis. Our data therefore suggests that MoMs are constantly recruited to the site of metastasis where they rapidly lose their immunostimulatory potential,

associated with the downregulation of antigen processing and presentation genes (*H2-Aa*, *Cd74*) and upregulation of the T cell inhibitory gene *Arg1* and the increased expression of M2 marker genes, *Chil3* and *Mrc1.*

In solid tumours, pan-macrophage targeted strategies using CSF-1 inhibitors as a single agent have shown very modest or no activity[14]. Since pan-macrophage targeted strategies will inevitably also remove immunostimulatory macrophages in PDAC liver metastasis, our findings support the rationale to develop more tailored approaches targeting immunosuppressive macrophage clusters or negative regulators controlling macrophage conversion towards an immunosuppressive subset.

While single-cell omics technology has advanced our understanding of macrophage heterogeneity, drivers of phenotypic and functional polarisation of macrophages in the metastatic microenvironment are still not fully elucidated. The presence of dead cells in the tumour microenvironment can induce an immunosuppressive state in macrophages[48]. However, conflicting evidence has been reported on the effect of dying cancer cells. While removal of dead cancer cells prevents inflammatory reaction, it may also suppress tumour antigen presentation by phagocytes[48]. In contrast, phagocytosis of apoptotic normal cells, a process known as efferocytosis, is a key mechanism during organ development and is generally accepted as tolerogenic[6,49]. In addition, the efferocytosis-mediated clearance of debris and dead cells by macrophages is a function that is pivotal to mitigate inflammation during the resolution phase and prevent tissue damage[6,49]. Thus, efferocytosis is physiologically used to protect from unwanted attack of the host tissues and result in a state of local immunosuppression in tissue. In the present study, we show that metastatic cancer cells hijack these evolutionary conserved and hard-wired pathways to create a local immunosuppressive microenvironment in the liver, thereby allowing disseminated cancer cells to escape immune detection and grow.

While tissue resident macrophages have been described to be more phagocytic than recruited MoMs[50], we show that MoMs accumulate at the necrotic sites and phagocytose dead resident cells. Reversal of this efferocytosis-induced immunosuppressive state can be achieved by

inhibiting phosphatidylserine receptor MerTK. Blockade of MerTK-mediated phagocytosis of dying cancer cells has previously been shown to suppress tumour growth in other types of cancers[51–54]. In one study, impaired macrophage mediated clearance of apoptotic cells by pharmacological blockade of MerTK increases the accumulation of dead cell bodies, resulting in the activation of STING pathway in macrophages via cGAMP/ATP[51]. In our studies, we already observed the activation of STING pathway in the absence of MerTK inhibition, which might be due to the overall high numbers of dead cells during metastasis induced liver injury. In agreement, liver injury induces STING pathway under non-cancerous conditions[55].

In addition to TAM receptors, such as MerTK, macrophages can bind apoptotic cells via STAB1 or TIM receptors, which include the resident macrophage marker TIM4[6]. Given the many variants of efferocytosis receptors, we therefore examined the effect of targeting the downstream phago-lysosomal pathway as an alternative strategy to suppress efferocytosis-induced immunosuppressive state in macrophages. Interestingly, uptake of extracellular accumulation of lipids has recently been shown to induce an immunosuppressive phenotype in macrophages[56]. Since engulfed lipids are processed through the lysosomal machinery, impairing lysosomal function may also inhibit lipid-induced macrophage conversion thereby representing an emerging checkpoint of macrophage functions.

Progranulin is a lysosomal protein associated with an immune regulation function[57]. We have previously shown that progranulin has pro-tumourigenic effects and activates fibroblasts in advanced PDAC liver metastasis[8]. In our present study, depletion of progranulin in efferocytic macrophages was sufficient to block upregulation of *Arg1* and restore T cell activation. Mechanistically, progranulin regulates the lysosomal acidification, via CFTR, that is required for optimal processing of apoptotic cell cargo and subsequent LXRα-mediated upregulation of *Arg1* (Fig. 7m). Consequently, CFTR or LXRα inhibition also result in macrophage conversion and T cell stimulation. Further studies will be needed to explore whether targeting efferocytosis (i.e. MerTK), lysosomal degradation (i.e. progranulin/CFTR), or downstream LXRα activation will be beneficial in combination with hepatotoxic chemotherapy, or in combination with

immune-checkpoint therapies to further harness the observed increased anti-tumour immune response.

In summary, our findings reveal that PDAC liver metastasis induces macrophage heterogeneity and that metastasis-promoting and restricting sub-clusters co-exist in metastatic livers. We also show that interfering with macrophage efferocytosis or its downstream signalling events inhibits macrophage immunosuppressive functions and restores anti-tumour immunity. Our findings therefore suggest that targeting macrophage efferocytosis may represent an attractive new treatment strategy for metastatic PDAC patients.

REFERENCES

1. Allemani, C. *et al.* Global surveillance of trends in cancer survival 2000–14 (CONCORD-3): analysis of individual records for 37 513 025 patients diagnosed with one of 18 cancers from 322 population-based registries in 71 countries. *Lancet* **391**, 1023–1075 (2018).
2. Ryan, D. P., Hong, T. S. & Bardeesy, N. Pancreatic adenocarcinoma. *N. Engl. J. Med.* **371**, 1039–1049 (2014).
3. Sinn, M. *et al.* CONKO-005: Adjuvant Chemotherapy With Gemcitabine Plus Erlotinib Versus Gemcitabine Alone in Patients After R0 Resection of Pancreatic Cancer: A Multicenter Randomized Phase III Trial. *J. Clin. Oncol.* **35**, 3330–3337 (2017).
4. Oettle, H. *et al.* Adjuvant chemotherapy with gemcitabine vs observation in patients undergoing curative-intent resection of pancreatic cancer: a randomized controlled trial. *JAMA* **297**, 267–277 (2007).
5. Conroy, T. *et al.* FOLFIRINOX or Gemcitabine as Adjuvant Therapy for Pancreatic Cancer. *N. Engl. J. Med.* **379**, 2395–2406 (2018).
6. Doran, A. C. Efferocytosis in health and disease. *Nat. Rev. Immunol.* **20**, (2020).
7. Green, D. R. The clearance of dead cells by efferocytosis. *Nat. Rev. Mol. Cell Biol.* **21**, (2020).
8. Nielsen, S. R. *et al.* Macrophage-secreted granulin supports pancreatic cancer metastasis by inducing liver fibrosis. *Nat. Cell Biol.* **18**, 549–560 (2016).
9. Tsilimigras, D. I. *et al.* Liver metastases. *Nat. Rev. Dis. Prim.* **7**, 27 (2021).
10. DeNardo, D. G. & Ruffell, B. Macrophages as regulators of tumour immunity and immunotherapy. *Nature Reviews Immunology* vol. 19 369–382 (2019).
11. Kitamura, T., Qian, B.-Z. & Pollard, J. W. Immune cell promotion of metastasis. *Nat. Rev. Immunol.* **15**, 73–86 (2015).
12. Doak, G. R., Schwertfeger, K. L. & Wood, D. K. Distant Relations: Macrophage Functions in the Metastatic Niche. *Trends in Cancer* **4**, 445–459 (2018).
13. Nielsen, S. R. & Schmid, M. C. Macrophages as Key Drivers of Cancer Progression and Metastasis. *Mediators Inflamm.* **2017**, 9624760 (2017).
14. Mantovani, A., Allavena, P., Marchesi, F. & Garlanda, C. Macrophages as tools and targets in cancer therapy. *Nature Reviews Drug Discovery* vol. 21 799–820 (2022).
15. Ma, R.-Y., Black, A. & Qian, B.-Z. Macrophage diversity in cancer revisited in the era of single-cell omics. *Trends Immunol.* **43**, 546–563 (2022).
16. Quaranta, V. *et al.* Macrophage-derived granulin drives resistance to immune

checkpoint inhibition in metastatic pancreatic cancer. *Cancer Res.* **78**, 4253–4269 (2018).
17. Wen, Y. Hepatic macrophages in liver homeostasis and diseases- diversity , plasticity and therapeutic opportunities. *Cell. Mol. Immunol.* (2021) doi:10.1038/s41423-020-00558-8.
18. Guilliams, M. *et al.* Spatial proteogenomics reveals distinct and evolutionarily conserved hepatic macrophage niches. *Cell* **185**, 379-396.e38 (2022).
19. Shi, C. & Pamer, E. G. Monocyte recruitment during infection and inflammation. *Nat. Rev. Immunol.* **11**, (2011).
20. Scott, C. L. *et al.* Bone marrow-derived monocytes give rise to self-renewing and fully differentiated Kupffer cells. 1–10 (2016) doi:10.1038/ncomms10321.
21. Lai, K. K. Y. *et al.* Stearoyl-CoA Desaturase Promotes Liver Fibrosis and Tumor Development in Mice via a Wnt Positive-Signaling Loop by Stabilization of Low-Density Lipoprotein-Receptor-Related Proteins 5 and 6. *Gastroenterology* **152**, 1477–1491 (2017).
22. Kazankov, K. *et al.* The role of macrophages in nonalcoholic fatty liver disease and nonalcoholic steatohepatitis. *Nat. Rev. Gastroenterol. Hepatol.* **16**, (2019).
23. Li, S. *et al.* Metabolism drives macrophage heterogeneity in the tumor microenvironment. *Cell Rep.* **39**, 110609 (2022).
24. Ben-Sasson, S. Z. *et al.* IL-1 enhances expansion, effector function, tissue localization, and memory response of antigen-specific CD8 T cells. *J. Exp. Med.* **210**, 491–502 (2013).
25. Mehta, A. K., Gracias, D. T. & Croft, M. TNF activity and T cells. *Cytokine* **101**, 14–18 (2018).
26. Cai, W. *et al.* STAT6/Arg1 promotes microglia/macrophage efferocytosis and inflammation resolution in stroke mice. *JCI insight* **4**, (2019).
27. Yurdagul, A. J. *et al.* Macrophage Metabolism of Apoptotic Cell-Derived Arginine Promotes Continual Efferocytosis and Resolution of Injury. *Cell Metab.* **31**, 518-533.e10 (2020).
28. Wu, Y.-M., Robinson, D. R. & Kung, H.-J. Signal pathways in up-regulation of chemokines by tyrosine kinase MER/NYK in prostate cancer cells. *Cancer Res.* **64**, 7311–7320 (2004).
29. Linger, R. M. A. *et al.* Mer or Axl receptor tyrosine kinase inhibition promotes apoptosis, blocks growth and enhances chemosensitivity of human non-small cell lung cancer. *Oncogene* **32**, 3420–3431 (2013).
30. Graham, D. K., Deryckere, D., Davies, K. D. & Earp, H. S. The TAM family: Phosphatidylserine-sensing receptor tyrosine kinases gone awry in cancer. *Nature Reviews Cancer* vol. 14 769–785 (2014).
31. Zhou, Y. *et al.* Blockade of the Phagocytic Receptor MerTK on Tumor-Associated Macrophages Enhances P2X7R-Dependent STING Activation by Tumor-Derived cGAMP. *Immunity* **52**, 357-373.e9 (2020).
32. Bhushan, B. *et al.* Pro-Regenerative Signaling after Acetaminophen-Induced Acute Liver Injury in Mice Identified Using a Novel Incremental Dose Model. *Am. J. Pathol.* **184**, 3013–3025 (2014).
33. Adhyapok, P. *et al.* A computational model of liver tissue damage and repair. *PLoS One* **15**, (2021).
34. Kao, A. W., McKay, A., Singh, P. P., Brunet, A. & Huang, E. J. Progranulin, lysosomal regulation and neurodegenerative disease. *Nat. Rev. Neurosci.* **18**, 325–333 (2017).
35. Yin, F. *et al.* Exaggerated inflammation, impaired host defense, and neuropathology in progranulin-deficient mice. *J. Exp. Med.* **207**, 117–128 (2010).
36. Hu, F. *et al.* Sortilin-mediated endocytosis determines levels of the frontotemporal dementia protein, progranulin. *Neuron* **68**, 654–667 (2010).
37. Chang, M. C. *et al.* Progranulin deficiency causes impairment of autophagy and TDP-43 accumulation. *J. Exp. Med.* **214**, 2611–2628 (2017).
38. Trzeciak, A., Wang, Y.-T. & Perry, J. S. A. First we eat, then we do everything else:

The dynamic metabolic regulation of efferocytosis. *Cell Metab.* **33**, 2126–2141 (2021).
39. Pourcet, B. & Pineda-Torra, I. LXR activation induces arginase 1 expression in macrophages. *Atherosclerosis* **213**, e7 (2010).
40. Repa, J. J. *et al.* Regulation of absorption and ABC1-mediated efflux of cholesterol by RXR heterodimers. *Science (80-.).* **289**, 1524–1529 (2000).
41. Cunha, L. D. *et al.* LC3-Associated Phagocytosis in Myeloid Cells Promotes Tumor Immune Tolerance. *Cell* **175**, 429-441.e16 (2018).
42. Lee, J. S., Badr, A., Eltobgy, M., Krause, K. & Hamilton, K. CFTR Modulators Restore Acidi fi cation of Autophago- Lysosomes and Bacterial Clearance in Cystic Fibrosis Macrophages. **12**, 1–21 (2022).
43. Di, A. *et al.* CFTR regulates phagosome acidification in macrophages and alters bactericidal activity. *Nat. Cell Biol.* **8**, 933–944 (2006).
44. Cheng, S. *et al.* A pan-cancer single-cell transcriptional atlas of tumor infiltrating myeloid cells. *Cell* **184**, 792-809.e23 (2021).
45. Zilionis, R. *et al.* Single-Cell Transcriptomics of Human and Mouse Lung Cancers Reveals Conserved Myeloid Populations across Individuals and Species. *Immunity* **50**, 1317-1334.e10 (2019).
46. Mulder, K. *et al.* Cross-tissue single-cell landscape of human monocytes and macrophages in health and disease. *Immunity* **54**, 1883-1900.e5 (2021).
47. Zhu, Y. *et al.* Tissue-Resident Macrophages in Pancreatic Ductal Adenocarcinoma Originate from Embryonic Hematopoiesis and Promote Tumor Progression. *Immunity* **47**, 323-338.e6 (2017).
48. DeNardo, D. G. & Ruffell, B. Macrophages as regulators of tumour immunity and immunotherapy. *Nat. Rev. Immunol.* **19**, 369–382 (2019).
49. Yin, C. & Heit, B. Cellular Responses to the Efferocytosis of Apoptotic Cells. *Front. Immunol.* **12**, 631714 (2021).
50. Roberts, A. W. *et al.* Tissue-Resident Macrophages Are Locally Programmed for Silent Clearance of Apoptotic Cells. *Immunity* **47**, 913-927.e6 (2017).
51. Zhou, Y. *et al.* Blockade of the phagocytic receptor MerTK on tumor-associated macrophages enhances P2X7R-dependent STING activation by tumor-derived cGAMP. *Immunity* **52**, 357–373 (2020).
52. Cook, R. S. *et al.* MerTK inhibition in tumor leukocytes decreases tumor growth and metastasis. *J. Clin. Invest.* **123**, 3231–3242 (2013).
53. Caetano, M. S. *et al.* Triple Therapy with MerTK and PD1 Inhibition Plus Radiotherapy Promotes Abscopal Antitumor Immune Responses. *Clin. cancer Res. an Off. J. Am. Assoc. Cancer Res.* **25**, 7576–7584 (2019).
54. Davra, V. *et al.* Axl and Mertk Receptors Cooperate to Promote Breast Cancer Progression by Combined Oncogenic Signaling and Evasion of Host Antitumor Immunity. *Cancer Res.* **81**, 698–712 (2021).
55. Chen, R., Du, J., Zhu, H. & Ling, Q. The role of cGAS-STING signalling in liver diseases. *JHEP reports Innov. Hepatol.* **3**, 100324 (2021).
56. Marelli, G. *et al.* Lipid-loaded macrophages as new therapeutic target in cancer. *J. Immunother. cancer* **10**, (2022).
57. Lan, Y.-J., Sam, N. B., Cheng, M.-H., Pan, H.-F. & Gao, J. Progranulin as a Potential Therapeutic Target in Immune-Mediated Diseases. *J. Inflamm. Res.* **14**, 6543–6556 (2021).
58. Hingorani, S. R. *et al.* Trp53R172H and KrasG12D cooperate to promote chromosomal instability and widely metastatic pancreatic ductal adenocarcinoma in mice. *Cancer Cell* **7**, 469–483 (2005).
59. Zhang, Y., Werling, U. & Edelmann, W. Seamless Ligation Cloning Extract (SLiCE) cloning method. *Methods Mol. Biol.* **1116**, 235–244 (2014).
60. Mederacke, I., Dapito, D. H., Affò, S., Uchinami, H. & Schwabe, R. F. High-yield and high-purity isolation of hepatic stellate cells from normal and fibrotic mouse livers. *Nat. Protoc.* **10**, 305–315 (2015).

MATERIALS AND METHODS

Detailed materials and methods can be found in the extended data section.

DATA AVAILABILITY

Mouse scRNA-seq were submitted to the Gene Expression Omnibus (GEO) repository and can be accessed under GEO accession no. GSE215118 (reviewer access token: wxobwseodxafryx). Human bulk RNA-seq data are available from the authors upon reasonable request and subsequent Data Transfer Agreement. All other data supporting the findings of this study are available from the corresponding author on reasonable request.

CODE AVAILABILITY

All code used to analyse data in this study is available on GitHub at https://github.com/CBFLivUni/Astuti_et_al_2023.

ACKNOWLEDGEMENTS

We thank the Liverpool Shared Research Facilities and the CRUK Beatson Institute Biological Science Unit for provision of equipment and technical assistance. We thank Elzbieta Boyd and Mark Glenn for technical support with molecular cloning and imaging acquisition and analysis. We thank research nurse Ruth Stafferton for consenting the patients. We also thank the patients and their families, as well as the healthy blood donors who contributed with tissue samples and blood donations to these studies. These studies were supported by grants from Cancer Research UK (A25607, A26978, A26979), Medical Research Council (MR/P018920/1) and North West Cancer Research Fund for M.C.S, Wellcome Trust (102521/Z/13/Z) and North West Cancer Research Fund for A.M., Cancer Research UK A17196, A2996, and A25233 for J.P.M.

AUTHOR CONTRIBUTIONS

Y.A. designed and performed most of the experiments, analysed and interpreted the data, and contributed to the preparation of the manuscript. M.R, V.Q, M.A, O. S., and G.B. helped with *in vivo* experiments, V.C.G helped with tissue section analysis, K.C. performed bioinformatic analysis. C.N. performed bulk RNA sequencing, F.C. helped with the analysis and interpretation of tumour biopsies. D.P., P.G., C.H., R.J. provided patient samples. J.W.P provided CSF-1R^{ERT}-Cre mice and conceptual advice. J.P.M. provided KPC mice and KPC-derived tissue samples. A.M. provided conceptual advice, interpreted data and wrote the manuscript. M.C.S. conceived and supervised the project, interpreted data, and wrote the manuscript. All authors critically analysed and approved the manuscript.

COMPETING INTERESTS

The authors declare no competing interests.

MAIN FIGURES AND MAIN FIGURE LEGENDS

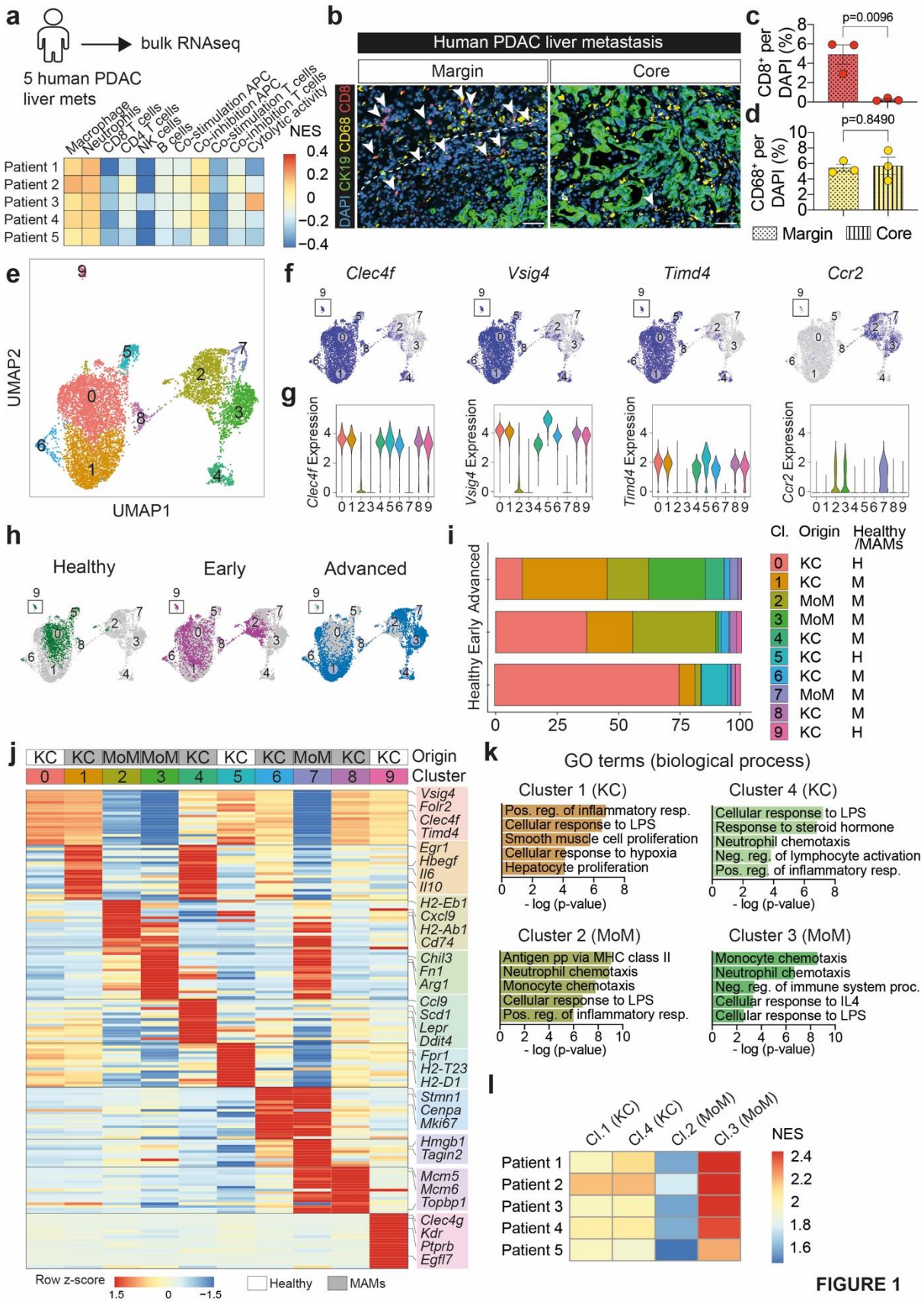
a
bulk RNAseq
5 human PDAC liver mets
Macrophage
Neutrophils
CD8 T cells
CD4 T cells
NK cells
B cells
Co-stimulation APC
Co-inhibition APC
Co-stimulation T cells
Co-inhibition T cells
Cytolytic activity
NES
Patient 1
Patient 2
Patient 3
Patient 4
Patient 5
b
Human PDAC liver metastasis
Margin
Core
DAPI CK19 CD68 CD8
c
p=0.0096
CD8+ per DAPI (%)
d
p=0.8490
CD68+ per DAPI (%)
Margin
Core
e
UMAP2
UMAP1
f
Clec4f
Vsig4
Timd4
Ccr2
g
Clec4f Expression
Vsig4 Expression
Timd4 Expression
Ccr2 Expression
h
Healthy
Early
Advanced
i
Healthy
Early
Advanced
Cl. Origin Healthy /MAMs
0 KC H
1 KC M
2 MoM M
3 MoM M
4 KC M
5 KC H
6 KC M
7 MoM M
8 KC M
9 KC H
j
Origin
Cluster
Vsig4
Folr2
Clec4f
Timd4
Egr1
Hbegf
Il6
Il10
H2-Eb1
Cxcl9
H2-Ab1
Cd74
Chil3
Fn1
Arg1
Ccl9
Scd1
Lepr
Ddit4
Fpr1
H2-T23
H2-D1
Stmn1
Cenpa
Mki67
Hmgb1
Tagin2
Mcm5
Mcm6
Topbp1
Clec4g
Kdr
Ptprb
Egfl7
Row z-score
Healthy
MAMs
k
GO terms (biological process)
Cluster 1 (KC)
Pos. reg. of inflammatory resp.
Cellular response to LPS
Smooth muscle cell proliferation
Cellular response to hypoxia
Hepatocyte proliferation
- log (p-value)
Cluster 4 (KC)
Cellular response to LPS
Response to steroid hormone
Neutrophil chemotaxis
Neg. reg. of lymphocyte activation
Pos. reg. of inflammatory resp.
- log (p-value)
Cluster 2 (MoM)
Antigen pp via MHC class II
Neutrophil chemotaxis
Monocyte chemotaxis
Cellular response to LPS
Pos. reg. of inflammatory resp.
- log (p-value)
Cluster 3 (MoM)
Monocyte chemotaxis
Neutrophil chemotaxis
Neg. reg. of immune system proc.
Cellular response to IL4
Cellular response to LPS
- log (p-value)
l
Cl.1 (KC)
Cl.4 (KC)
Cl.2 (MoM)
Cl.3 (MoM)
NES
Patient 1
Patient 2
Patient 3
Patient 4
Patient 5

FIGURE 1

Figure 1. Identification of diverse metastasis-associated macrophage populations in metastatic PDAC livers by combining single cell analysis with spatial in-situ labelling strategy

(a) Graphical schematics of bulk RNAseq on fresh liver metastasis biopsies from chemotherapy-naïve PDAC patients (n=5) (top) and heatmap showing scores (normalised enrichment score; ssGSEA) for immune signatures (bottom).

(b-d) Representative immunofluorescence images of human PDAC liver metastasis (n= 3) at the tumour margin (left image, dashed line) and in the core of the tumour (right image) showing that peripheral regions are rich in macrophages ($CD68^+$, yellow) and cytotoxic T cells ($CD8^+$, red), while core regions are rich in macrophages but lack T cells. Metastatic pancreatic cancer cells stained for cytokeratin ($CK19^+$, green), nuclei were counterstained with DAPI (blue). Arrowheads indicate $CD8^+$ T cells. Scale bars 50 µm. Quantification of $CD8^+$ T cells **(c)** and macrophages ($CD68^+$ cells) **(d)** in the tumour margin and core as depicted in **(b)**. Data are presented as mean ± SEM. Statistical analysis was performed using unpaired t-test.

(e) UMAP plot identifying 10 clusters within macrophages ($F4/80^+$) isolated by flow cytometry from healthy liver, early metastatic livers (d5) and advanced metastatic livers (d10) induced by intra-portal implantation of KPC-derived cells into mice with established orthotopic PDAC tumours (9171 $F4/80^+$ cells, sorted from n=3 mice/group).

(f) UMAP plots depicting expression of common markers of Kupffer cells (KCs) (*Clec4f*, *Vsig4*, and *Timd4*) and monocyte-derived macrophages (MoMs) (*Ccr2*).

(g) Violin plots depicting expression levels of common markers of Kupffer cells (KCs) (*Clec4f*, *Vsig4*, and *Timd4*) and monocyte-derived macrophages (MoMs) (*Ccr2*) in clusters 0-9.

(h) UMAP plots depicting distribution of different macrophage clusters in healthy livers, early metastatic livers (d5), and advanced metastatic livers (d10).

(i) Proportions of each macrophage cluster in healthy, early metastasis, and advanced metastasis.

(j) Heatmap depicting relative average expression of the top upregulated differentially expressed genes in each macrophage cluster compared to all other clusters in the dataset. Representative genes are labelled for each cluster.

(k) Enriched biological processes (Gene Ontology, GOBP) in major MAM clusters derived from KC (cluster 1 and 4) and monocytes (cluster 2 and 3).

(l) Heatmap showing signature scores (normalised enrichment score (NES); ssGSEA) of major KC-MAM and Mo-MAM clusters in human PDAC liver metastasis samples (n=5 patients).

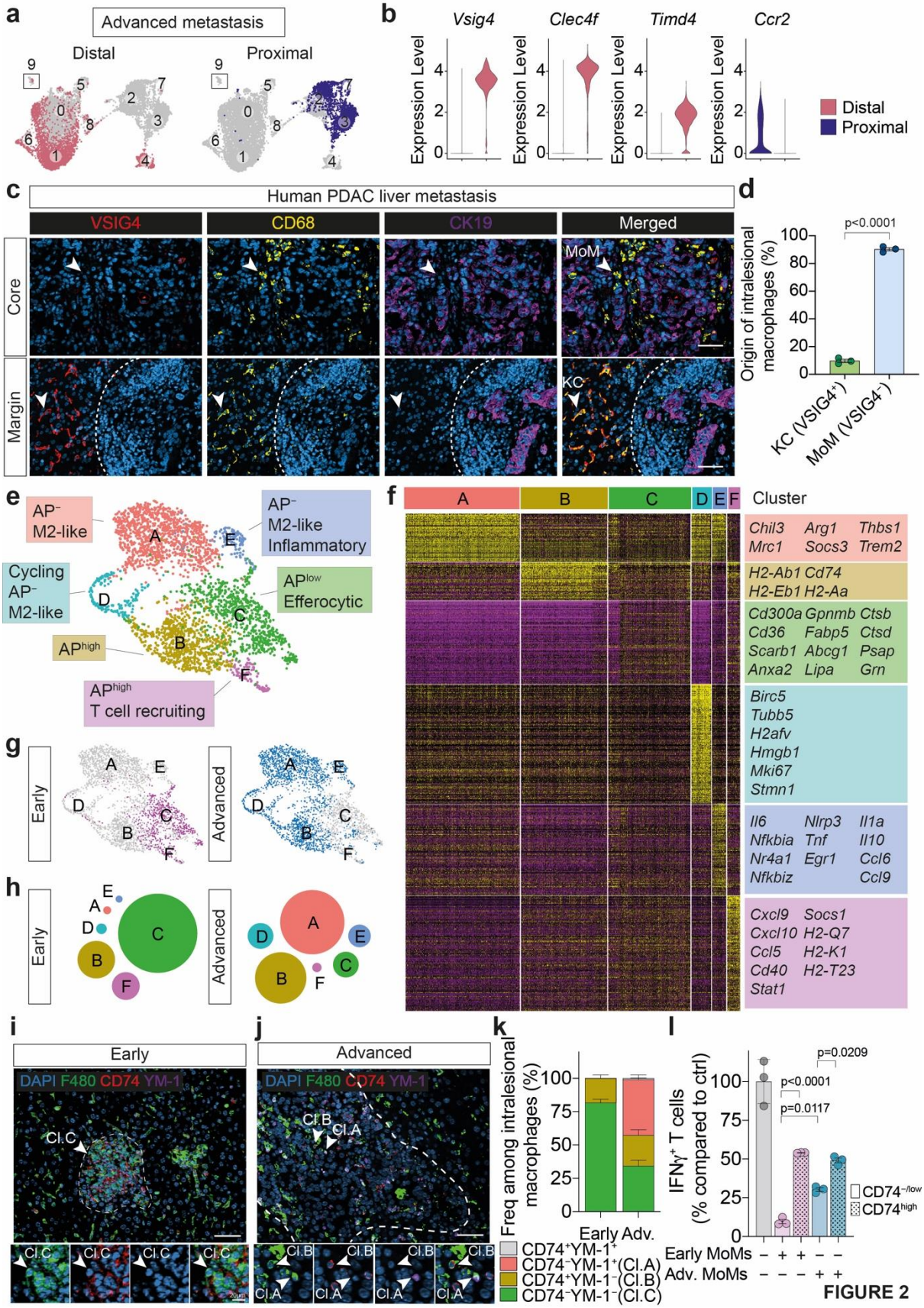
a
Advanced metastasis
Distal
Proximal
b
Vsig4
Clec4f
Timd4
Ccr2
Expression Level
Distal
Proximal
c
Human PDAC liver metastasis
VSIG4
CD68
CK19
Merged
Core
Margin
MoM
KC
d
p<0.0001
Origin of intralesional macrophages (%)
KC (VSIG4+)
MoM (VSIG4-)
e
AP- M2-like
AP- M2-like Inflammatory
Cycling AP- M2-like
APlow Efferocytic
APhigh
APhigh T cell recruiting
f
Cluster
Chil3 Arg1 Thbs1
Mrc1 Socs3 Trem2
H2-Ab1 Cd74
H2-Eb1 H2-Aa
Cd300a Gpnmb Ctsb
Cd36 Fabp5 Ctsd
Scarb1 Abcg1 Psap
Anxa2 Lipa Grn
Birc5
Tubb5
H2afv
Hmgb1
Mki67
Stmn1
Il6 Nlrp3 Il1a
Nfkbia Tnf Il10
Nr4a1 Egr1 Ccl6
Nfkbiz Ccl9
Cxcl9 Socs1
Cxcl10 H2-Q7
Ccl5 H2-K1
Cd40 H2-T23
Stat1
g
Early
Advanced
h
Early
Advanced
i
Early
DAPI F480 CD74 YM-1
Cl.C
j
Advanced
DAPI F480 CD74 YM-1
Cl.B
Cl.A
k
Freq among intralesional macrophages (%)
Early Adv.
CD74+YM-1+
CD74-YM-1+(Cl.A)
CD74+YM-1-(Cl.B)
CD74-YM-1-(Cl.C)
l
IFNγ+ T cells (% compared to ctrl)
p=0.0209
p<0.0001
p=0.0117
CD74-/low
CD74high
Early MoMs
Adv. MoMs

FIGURE 2

Figure 2. CD74$^{neg/low}$ MoMs display potent immunosuppressive functions at an early metastatic stage

(a) UMAP plots showing distribution of proximal MAMs (pMAMs) and distal MAMs (dMAMs) in advanced metastatic tumours (d10) based on in-situ labelling.

(b) Violin plots depicting expression levels of KC (*Vsig4, Clec4f*, *Timd4*) and MoM (*Ccr2*) genes in pMAMs and dMAMs identifying MoMs (*Ccr2*$^{+}$) as the main proximal macrophage cluster.

(c) Representative immunofluorescent images of tumour core areas (upper row) and margin areas (lower row, dashed line) of liver metastasis derived from PDAC patients (n=3). Pan-macrophages were identified by CD68 (yellow), KC by VSIG4^{+} (red), and disseminated cancer cells by CK19 (purple), nuclei were counterstained with DAPI (blue). Scale bar 50 µm.

(d) Quantification of MoMs (VSIG4^{-}) and KCs (VSIG4^{+}) among intralesional/core macrophages as shown in **(c)**. Data are presented as mean ± SEM. Statistical analysis was performed using unpaired t-test.

(e) UMAP plot identifying 6 clusters of MoMs derived from cluster 2, 3, and 7 in the original UMAP (Fig. 1c).

(f) Heatmap depicting relative average expression of upregulated differentially expressed genes in each MoM cluster compared to all other MoM clusters in the dataset. Representative genes are labelled for each cluster.

(g) UMAP plots depicting distribution of MoM clusters in early (d5) and advanced metastatic livers (d10).

(h) Diagrams showing distribution of MoM clusters in early (d5) and advanced metastatic livers (d10).

(i-k) Representative immunofluorescent images of early **(i)** and advanced **(j)** liver metastasis derived from experimental intrasplenic model (n=3 mice/group). Pan-macrophages were identified by F480 (green), antigen presentation marker CD74 (red), and M2 marker YM-1 (purple), nuclei were counterstained with DAPI (blue). Scale bar 50 µm. **(k)** Quantification of staining showing percentages of intralesional macrophages resembling major MoM clusters: cluster C-like (CD74^{-}YM-1^{-}), cluster B-like (CD74^{+}YM-1^{-}), and cluster A-like (CD74^{-}YM-1^{+}). Data are presented as mean ± SEM.

(l) Relative CD8^{+} T cell activation measured by percentages of IFNγ^{+} CD8^{+} T-cells following stimulation with anti-CD3/CD28-coupled Dynabeads and co-culture with FACS-sorted early or advanced MoMs (F4/80^{+}TIM4^{-}) from experimental intrasplenic model compared to Dynabeads-only control (n=3 biological replicates/group). Data are presented as mean ± SEM. Statistical analysis was performed using one-way ANOVA with Sidak's post-test.

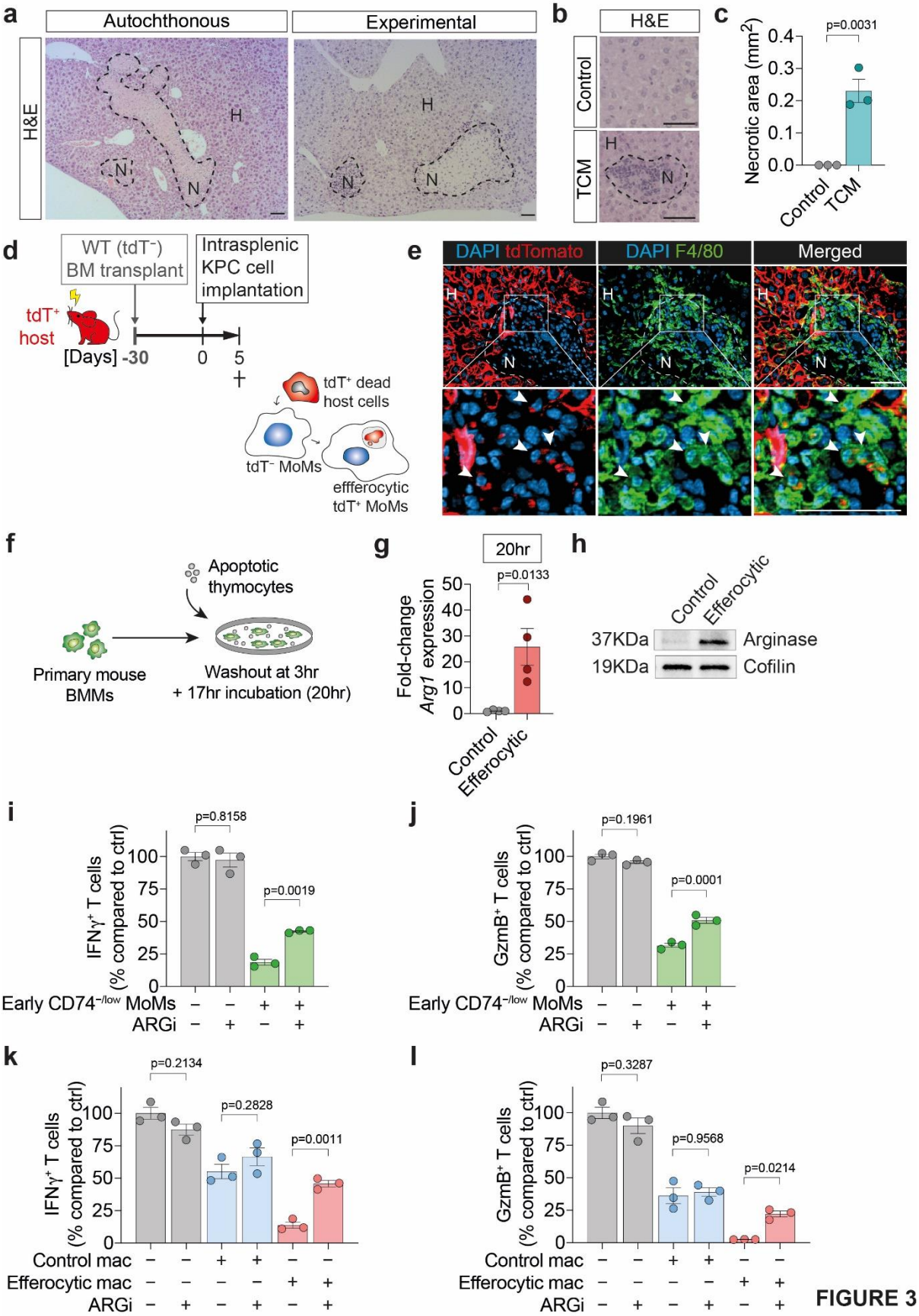
a
Autochthonous
Experimental
H&E
H
N
b
H&E
Control
TCM
c
Necrotic area (mm2)
p=0.0031
Control
TCM
d
WT (tdT−) BM transplant
Intrasplenic KPC cell implantation
tdT+ host
[Days] -30
0
5
tdT+ dead host cells
tdT− MoMs
effferocytic tdT+ MoMs
e
DAPI tdTomato
DAPI F4/80
Merged
f
Apoptotic thymocytes
Primary mouse BMMs
Washout at 3hr + 17hr incubation (20hr)
g
20hr
p=0.0133
Fold-change Arg1 expression
Control
Efferocytic
h
Control
Efferocytic
37KDa
Arginase
19KDa
Cofilin
i
p=0.8158
p=0.0019
IFNγ+ T cells (% compared to ctrl)
Early CD74−/low MoMs
ARGi
j
p=0.1961
p=0.0001
GzmB+ T cells (% compared to ctrl)
Early CD74−/low MoMs
ARGi
k
p=0.2134
p=0.2828
p=0.0011
IFNγ+ T cells (% compared to ctrl)
Control mac
Efferocytic mac
ARGi
l
p=0.3287
p=0.9568
p=0.0214
GzmB+ T cells (% compared to ctrl)
Control mac
Efferocytic mac
ARGi

FIGURE 3

Figure 3. Tissue resident cell death triggers efferocytosis-mediated macrophage conversion to an immunosuppressive phenotype

(a) Representative H&E images of hepatic necroses in autochthonous KPC mice with pre-metastatic PDAC (left) and 48 hours post intrasplenic implantation of KPC cells in wildtype mice (right). Dotted lines demarcate the necrotic areas (N = necrotic, H = healthy) (n=3 mice/group). Scale bar 50 µm.

(b-c) KPC cell culture derived tumour-conditioned medium (TCM) or control DMEM medium (Control) was injected into the tail vein of wildtype mice once daily for 3 days. Livers were harvested 24 hour post last media injection (n=3 mice/group).

(b) Representative H&E images of the livers in mice following treatment with TCM or DMEM control (Control). Dotted line demarcates the necrotic area. Scale bar 50 µm.

(c) Quantification of hepatic necroses size as depicted in **(b)**. Data are presented as mean ± SEM. Statistical analysis was performed using unpaired t-test.

(d-e) Chimeric mice were generated via bone marrow (BM) transplantation resulting in dtTomatoRed-expressing (tdT^+) hosts cells and non-labelled (tdT^-) bone marrow/monocyte derived macrophages (MoMs), followed by intrasplenic implantation of KPC cells (n=3 mice). Livers were harvested 5 days post implantation.

(d) Graphical schematics of the experiment.

(e) Representative immunofluorescent images of MoMs ($F4/80^+tdTomato^-$) in healing necrotic areas. $tdTomato^+$ debris-containing MoMs are indicated by the arrowheads. N = necrotic, H = healthy areas. Scale bar 50 µm.

(f) Graphical schematic of efferocytosis assay in mouse primary bone marrow-derived macrophages (BMMs).

(g) Fold expression of *Arg1* assessed by qPCR in mouse primary BMM following 3-hour co-culture with apoptotic thymocytes and further 17-hour incubation (efferocytic) vs non-treated control (n=3 biological replicates/group). Data are presented as mean ± SEM. Statistical analysis was performed using unpaired t-test.

(h) Representative Western blot image of arginase 1 and loading control cofilin levels in control and efferocytic BMMs following 3-hour co-culture with apoptotic thymocytes and further 17-hour incubation (experiment was performed three times with similar results).

(i-j) Relative CD8+ T cell activation measured by percentages of $IFN\gamma^+$ **(i)** or granzyme B $(GzmB)^+$ **(k)** $CD8^+$ T-cells following stimulation with anti-CD3/CD28-coupled Dynabeads and co-culture with $CD74^{-/low}$ MoMs isolated from the early stage of metastasis with or without arginase inhibitor, CB-1158 (ARGi) compared to Dynabeads-only control (n=3 biological replicates/group). Data are presented as mean ± SEM. Statistical analysis was performed using one-way ANOVA with Sidak's post-test.

(k-l) Relative $CD8^+$ T cell activation measured by percentages $IFN\gamma^+$ **(k)** or granzyme B $(GzmB)^+$ **(l)** $CD8^+$ T-cells following stimulation with anti-CD3/CD28-coupled Dynabeads and co-culture with efferocytic BMMs (post 4-hour incubation with apoptotic thymocytes) with or without arginase inhibitor, CB-1158 (ARGi) compared to Dynabeads-only control (n=3 biological replicates/group). Data are presented as mean ± SEM. Statistical analysis was performed using one-way ANOVA with Sidak's post-test.

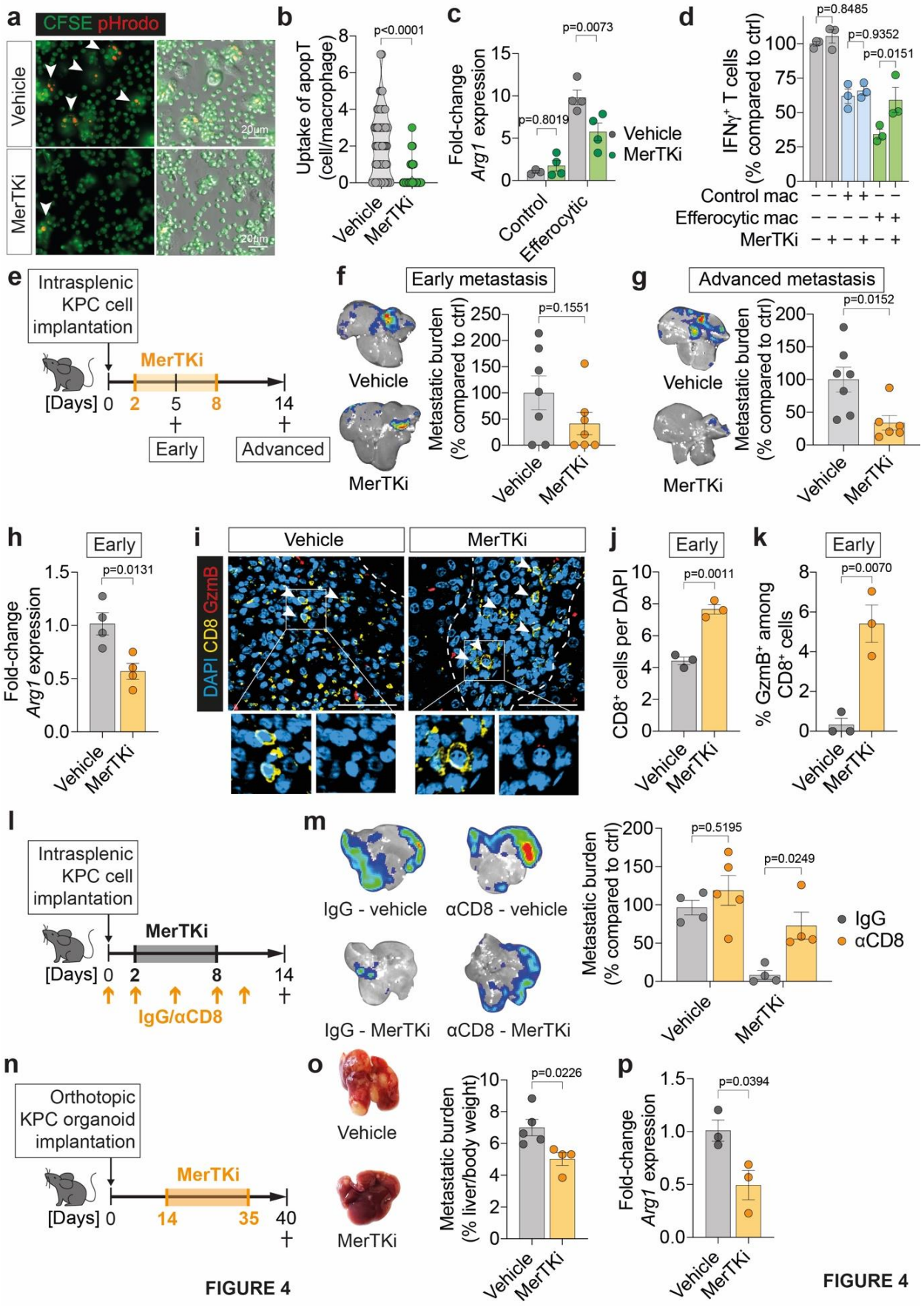

FIGURE 4

FIGURE 4

Figure 4. Inhibition of efferocytosis prevents Mo-MAM conversion and PDAC metastasis

(a, b) Mouse BMMs were incubated for 5 hours with pHrodo/CFSE-labelled apoptotic murine thymocytes (apopT) in the presence or absence of MerTK inhibitor UNC2250 (MerTKi). Representative fluorescence image (**a**) and quantification of engulfed apopT in BMMs (**b**) (vehicle n=65 cells; MerTKi n=112 cells), experiment was performed twice with similar results). Data are presented as mean ± SEM. Statistical analysis was performed using unpaired t-test.

(c) Fold expressions of *Arg1* as assessed by qPCR in BMMs following incubation for 20 hours with apoptotic thymocytes (efferocytic) compared to control with or without MerTKi (Control/vehicle n=3, Control/MerTKi n=4, Efferocytic/vehicle n=4, Efferocytic/MerTKi n=4 biological replicates). Data are presented as mean ± SEM. Statistical analysis was performed using two-way ANOVA with Sidak's post-test.

(d) Relative $CD8^+$ T cell activation measured by percentages of $IFN\gamma^+$ $CD8^+$ T-cells following stimulation with anti-CD3/CD28-coupled Dynabeads and co-culture with efferocytic BMMs (post 4-hour incubation with apoptotic thymocytes) with or without MerTKi compared to Dynabeads-only control (n=3 biological replicates/group). Data are presented as mean ± SEM. Statistical analysis was performed using one-way ANOVA with Sidak's post-test.

(e-k) Liver metastasis was induced by intrasplenic implantation of $KPC^{Luc/ZsGreen}$ cells. Oral administration of 10mg/kg MerTKi or vehicle control was given daily from day 2 to 8 post implantation. Early (d5) and advanced (d14) metastatic livers were resected and analysed.

(e) Schematic diagram illustrating the MerTKi experiment timeline.

(f) Representative *ex vivo* bioluminescence imaging (BLI) images (left) and relative total flux (% tumour burden, right) of early metastatic livers (d5) from mice treated with MerTKi compared to control (n=7 mice/group). Data are presented as mean ± SEM. Statistical analysis was performed using unpaired t-test.

(g) Representative *ex vivo* bioluminescence imaging (BLI) images (left) and relative total flux (% tumour burden, right) of advanced metastatic livers (d14, endpoint) from mice treated with MerTKi compared to control (control n=7 mice; MerTKi n=6 mice). Data are presented as mean ± SEM. Statistical analysis was performed using unpaired t-test.

(h) Fold expression of *Arg1* in MoMs ($F4/80^+TIM4^-$) isolated from early metastatic tumour from mice treated with vehicle or MerTKi as assessed by qPCR (n=4 mice/group). Data are presented as mean ± SEM. Statistical analysis was performed using unpaired t-test.

(i, j) Representative immunofluorescence images (**i**) and quantification of intralesional $CD8^+$ T-cells (**j**) and percentage of cytotoxic granzyme B $(GzmB)^+$ T cells **(k)** in early metastatic lesions from mice treated with vehicle or MerTKi. Arrowheads indicate $CD8^+$ T cells (yellow), nuclei were counterstained with DAPI (blue) (n=3 mice/group). Scale bars 50 µm. Data are presented as mean ± SEM. Statistical analysis was performed using unpaired t-test.

(l-n) Liver metastasis was induced by intrasplenic implantation of $KPC^{Luc/ZsGreen}$ cells. Oral administration of 10mg/kg MerTKi or vehicle control was given daily from day 2 to 8 post implantation. Anti-mouse CD8α or IgG2b isotype control was given at 100μg per mouse every 3 days. Advanced (d14) metastatic livers were resected and analysed.

(l) Schematic diagram illustrating the MerTKi +/- CD8 depletion experiment timeline.

(m) Representative *ex vivo* bioluminescence imaging (BLI) images (left) and relative total flux (% tumour burden, right) of advanced metastatic livers (d14) from mice treated with MerTKi compared to control (vehicle/IgG n=4 mice, vehicle/αCD8 n=5 mice, MerTKi/IgG n=4 mice, MerTKi/αCD8 n=4 mice). Data are presented as mean ± SEM. Statistical analysis was performed using two-way ANOVA with Sidak's posthoc test.

(n-p) Spontaneous liver metastasis was induced by pancreatic implantation of KPC organoids. Oral administration of 10mg/kg MerTKi or vehicle control was given every 3 days from day 14 to 35 post implantation.

(n) Schematic diagram illustrating the MerTKi in spontaneous liver metastasis experiment timeline.

(o) Representative liver photographs (left) and tumour burden of advanced metastatic livers from mice treated with MerTKi compared to control (control n=5 mice, MerTKi n=4 mice). Data are presented as mean ± SEM. Statistical analysis was performed using unpaired t-test.

(p) Fold expression of *Arg1* in MoMs ($F4/80^{+}TIM4^{-}$) isolated from advanced metastatic tumour from mice treated with vehicle or MerTKi as assessed by qPCR (n=3 mice/group). Data are presented as mean ± SEM. Statistical analysis was performed using unpaired t-test.

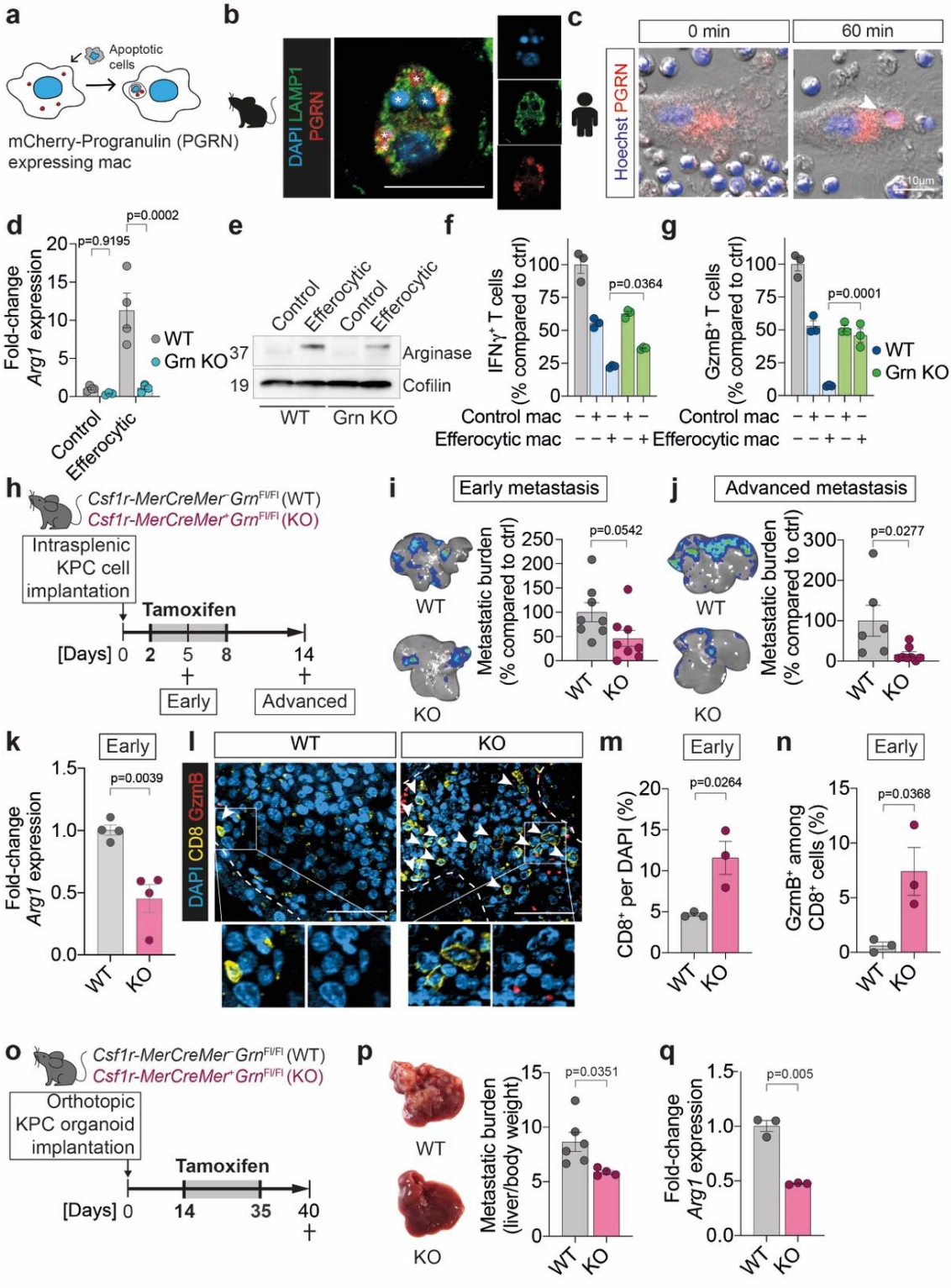
a
Apoptotic cells
mCherry-Progranulin (PGRN) expressing mac
b
DAPI LAMP1 PGRN
c
0 min
60 min
Hoechst PGRN
10µm
d
p=0.0002
p=0.9195
Fold-change Arg1 expression
WT
Grn KO
Control
Efferocytic
e
Control
Efferocytic
Control
Efferocytic
37
19
Arginase
Cofilin
WT
Grn KO
f
IFNγ+ T cells (% compared to ctrl)
p=0.0364
Control mac
Efferocytic mac
g
GzmB+ T cells (% compared to ctrl)
p=0.0001
WT
Grn KO
h
Csf1r-MerCreMer-Grn Fl/Fl (WT)
Csf1r-MerCreMer+Grn Fl/Fl (KO)
Intrasplenic KPC cell implantation
Tamoxifen
[Days] 0 2 5 8 14
Early
Advanced
i
Early metastasis
WT
KO
Metastatic burden (% compared to ctrl)
p=0.0542
j
Advanced metastasis
p=0.0277
k
Early
p=0.0039
Fold-change Arg1 expression
l
WT
KO
DAPI CD8 GzmB
m
Early
p=0.0264
CD8+ per DAPI (%)
n
Early
p=0.0368
GzmB+ among CD8+ cells (%)
o
Csf1r-MerCreMer-Grn Fl/Fl (WT)
Csf1r-MerCreMer+Grn Fl/Fl (KO)
Orthotopic KPC organoid implantation
Tamoxifen
[Days] 0 14 35 40
p
WT
KO
Metastatic burden (liver/body weight)
p=0.0351
q
p=0.005
Fold-change Arg1 expression

FIGURE 5

Figure 5. Depletion of progranulin prevents macrophage conversion and reduces PDAC liver metastasis

(a-c) Mouse BMMs or human primary macrophages were transduced with mCherry-mPGRN (mCherry-tagged progranulin) construct to track proganulin localisation. mCherry-PGRN-expressing macrophages were then incubated with apoptotic thymocytes or primary human lymphocytes, respectively.

(a) Schematic of the progranulin localisation assay in mouse or human macrophages.

(b) Representative immunofluorescence image depicting co-localisation of mCherry-PGRN with phagocytosed apoptotic thymocytes (nuclei indicated by asterisks) (n>30 cells, experiment was performed twice with similar results). Scale bar 50 μm.

(c) Representative fluorescence image depicting localisation of mCherry-PGRN with phagosomes containing phagocytosed apoptotic lymphocyte (arrowhead) over time as assessed by live cell imaging (experiment was performed twice with similar results).

(d) Fold expression of *Arg1* as assessed by qPCR in unstimulated and efferocytic (incubated with apoptotic thymocytes) WT or Grn KO BMMs (n=4 biological replicates /group). Data are presented as mean ± SEM. Statistical analysis was performed using two-way ANOVA with Sidak's post-test.

(e) Representative Western blot image of arginase 1 and loading control cofilin levels in control and efferocytic WT or Grn KO BMMs following 3-hour co-culture with apoptotic thymocytes and further 17-hour incubation (experiment was performed three times with similar results).

(f-g) Relative $CD8^+$ T cell activation measure by percentages of $IFN\gamma^+$ **(f)** or granzyme B $(GzmB)^+$ **(g)** $CD8^+$ T cells following stimulation with anti-CD3/CD28-coupled Dynabeads and co-culture with control (unstimulated) or efferocytic (incubated with apoptotic thymocytes) WT or Grn KO BMMs compared to Dynabeads-only control (n=3 biological replicates /group). Data are presented as mean ± SEM. Statistical analysis was performed using one-way ANOVA with Sidak's post-test.

(h-n) Liver metastasis was induced in mice lacking progranulin expression in macrophages (*Csf1r-Cre*$^{+/+}$ or $^{+/-}$ *Grn*$^{fl/fl}$; KO) and control mice with progranulin expression in macrophages (*Cre*$^{-/-}$*Grn*$^{fl/fl}$; WT) by intrasplenic implantation of KPC$^{Luc/ZsGreen}$ cells. Both groups were given oral doses of tamoxifen (50mg/kg) from day 2 to 8 after implantation. Early (d5) and advanced (d14) metastatic livers were resected and analysed.

(h) Schematic diagram illustrating the tumour study using mice with conditional depletion of progranulin in macrophages (KO).

(i) Representative *ex vivo* bioluminescence imaging (BLI) images (left) and relative total flux (% tumour burden, right) of early metastatic livers (d5) from KO compared to WT mice (n=8

mice/group). Data are presented as mean ± SEM. Statistical analysis was performed using unpaired t-test.

(j) Representative *ex vivo* bioluminescence imaging (BLI) images (left) and relative total flux (% tumour burden, right) of advanced metastatic livers (d14, endpoint) from KO compared to WT mice (WT n=6 mice; KO n=8 mice). Data are presented as mean ± SEM. Statistical analysis was performed using unpaired t-test.

(k) Fold expression of *Arg1* early MoMs ($F4/80^{+}TIM4^{-}$) from KO compared to WT mice as assessed by qPCR (n=4 mice/group). Data are presented as mean ± SEM. Statistical analysis was performed using unpaired t-test.

(l-n) Representative immunofluorescence images (**l**) and quantification of $CD8^{+}$ T-cells (**m**) and percentage of cytotoxic granzyme B $(GzmB)^{+}$ T cells in early metastasis from WT or KO mice. Arrowheads indicate $CD8^{+}$ T cells (yellow), nuclei were counterstained with DAPI (blue) (n=3 mice/group). Scale bars 50 µm. Data are presented as mean ± SEM. Statistical analysis was performed using unpaired t-test.

(o-q) Spontaneous liver metastasis was induced by pancreatic implantation of KPC organoids. Oral administration of tamoxifen (50mg/kg) was given every 3 days from day 14 to 35 post implantation.

(o) Schematic diagram illustrating the timeline of spontaneous liver metastasis study using mice with conditional depletion of progranulin in macrophages (KO).

(p) Representative liver photographs (left) and tumour burden of advanced metastatic livers from KO compared to WT (WT n=6 mice; KO n=4 mice). Data are presented as mean ± SEM. Statistical analysis was performed using unpaired t-test.

(q) Fold expression of *Arg1* in MoMs ($F4/80^{+}TIM4^{-}$) isolated from advanced metastatic tumour from WT or KO mice as assessed by qPCR (n=3 mice/group). Data are presented as mean ± SEM. Statistical analysis was performed using unpaired t-test.

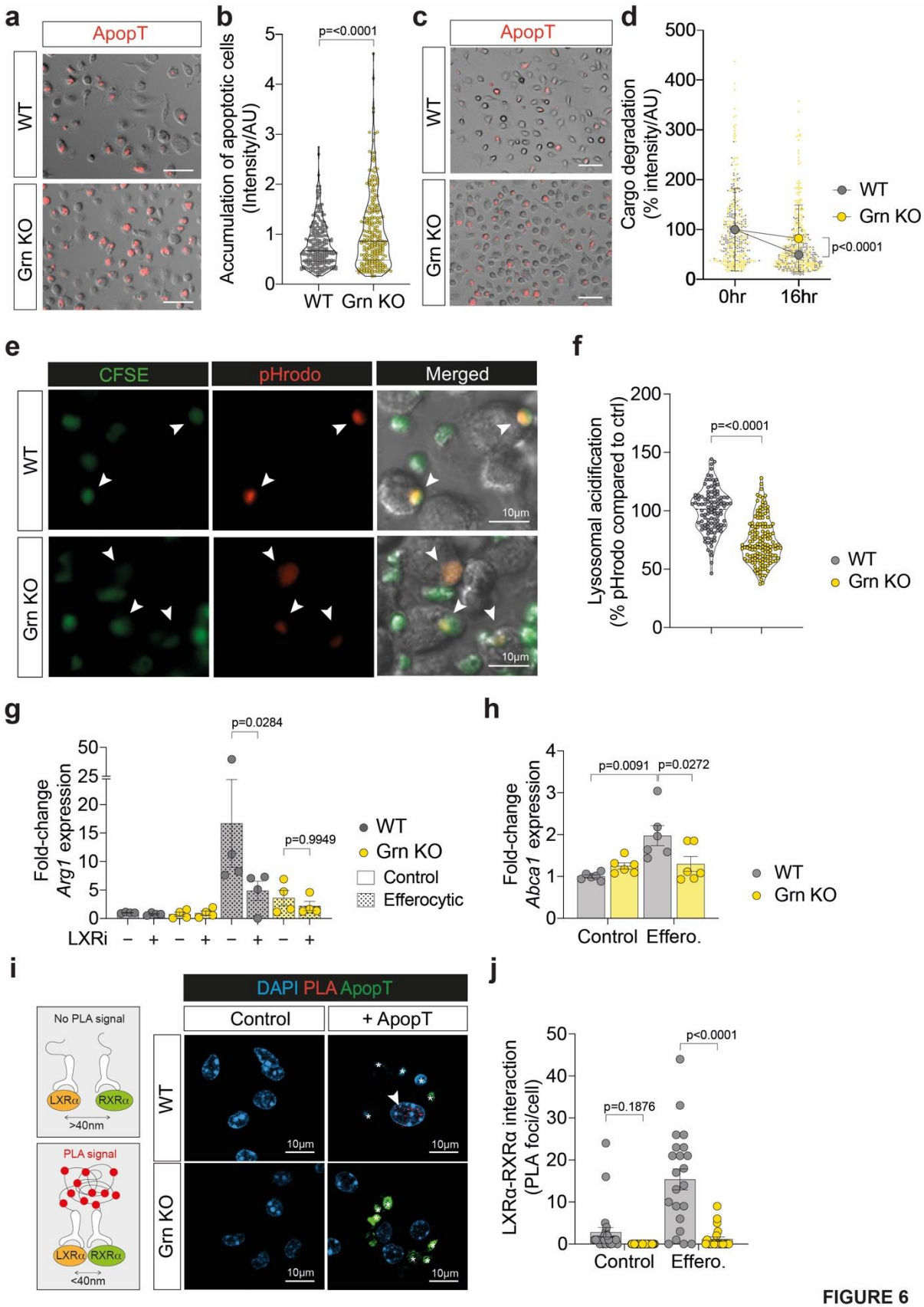
a
ApopT
WT
Grn KO
b
Accumulation of apoptotic cells (Intensity/AU)
p=<0.0001
WT
Grn KO
c
ApopT
WT
Grn KO
d
Cargo degradation (% intensity/AU)
WT
Grn KO
p<0.0001
0hr
16hr
e
CFSE
pHrodo
Merged
WT
Grn KO
10μm
f
Lysosomal acidification (% pHrodo compared to ctrl)
p=<0.0001
WT
Grn KO
g
Fold-change Arg1 expression
p=0.0284
p=0.9949
WT
Grn KO
Control
Efferocytic
LXRi
h
Fold-change Abca1 expression
p=0.0091
p=0.0272
WT
Grn KO
Control
Effero.
i
DAPI PLA ApopT
Control
+ ApopT
No PLA signal
LXRα
RXRα
>40nm
PLA signal
<40nm
WT
Grn KO
10μm
j
LXRα-RXRα interaction (PLA foci/cell)
p=0.1876
p<0.0001
Control
Effero.

FIGURE 6

Figure 6. Progranulin deficiency impairs lysosomal acidification and cargo degradation during efferocytosis

(a, b) Representative fluorescence image (**a**) of mouse WT or Grn KO BMMs 20 hours after adding red CellTrace-labelled apoptotic thymocytes (ApopT) and quantification (**b**) of their uptake (n≥150 cells/group, experiment was performed twice with similar results). Data are presented as mean ± SEM from one experiment. Statistical analysis was performed using unpaired t-test. Scale bars 50 μm.

(c, d) As described in a,b, but after 3 hours, macrophages were thoroughly washed to remove remaining ApopT and decays in red CellTrace-labelled apoptotic thymocytes signal intensity were analysed 16 hours later. Representative images at endpoint (16h) (**c**) and quantification of the data (**d**) (n≥150 cells/group, experiment was performed twice with similar results). Data are presented as mean ± SEM from one experiment. Statistical analysis was performed using unpaired t-test. Scale bars 50μm.

(e, f) WT or Grn KO BMMs were incubated with pHrodo/CFSE-labelled apoptotic thymocytes (ApopT) and analysed by live cell imaging for 5 hours. Representative fluorescence images (**e**) at peak of pHrodo intensity (arrowheads) and quantification (**f**) (WT n=115 cells; Grn KO n=164 cells, experiment was performed three times with similar results). Data are presented as mean ± SEM. Statistical analysis was performed using unpaired t-test.

(g) Fold expressions of *Arg1* as assessed by qPCR in WT or Grn KO BMMs following incubation for 20 hours with apoptotic thymocytes (efferocytic) compared to control with or without LXRα inhibitor, GSK-2033 (LXRi) (n=4 biological replicates/group). Data are presented as mean ± SEM. Statistical analysis was performed using two-way ANOVA with Sidak's post-test.

(h) Fold change in the expression of LXRα target gene *Abca1* as assessed by qPCR in WT or Grn KO BMMs following 20-hour incubation with apoptotic thymocytes (ApopT) (n=6 biological replicates/group). Data are presented as mean ± SEM. Statistical analysis was performed using two-way ANOVA with Tukey's post-test.

(i, j) Schematic (**i**) of proximity ligation assay (PLA) for LXRα and RXRα (left) and representative fluorescence images (right) of PLA probe-bound fluorophore (PLA, red) in WT or Grn KO BMMs following 4-hour incubation with CFSE-labelled apoptotic thymocytes (ApopT, green). Nuclei were counterstained with DAPI (blue). Asterisks indicate phagocytosed apoptotic cells. Quantification (**j**) of PLA foci (arrowhead) in WT or Grn KO BMMs as depicted in (**i**) (control WT n=24 cells, control Grn KO n=32 cells, efferocytic WT n=22 cells, efferocytic Grn KO n=22 cells, experiment was repeated three times with similar results). Data are presented as mean ± SEM. Statistical analysis was performed using two-way ANOVA with Sidak's post-test.

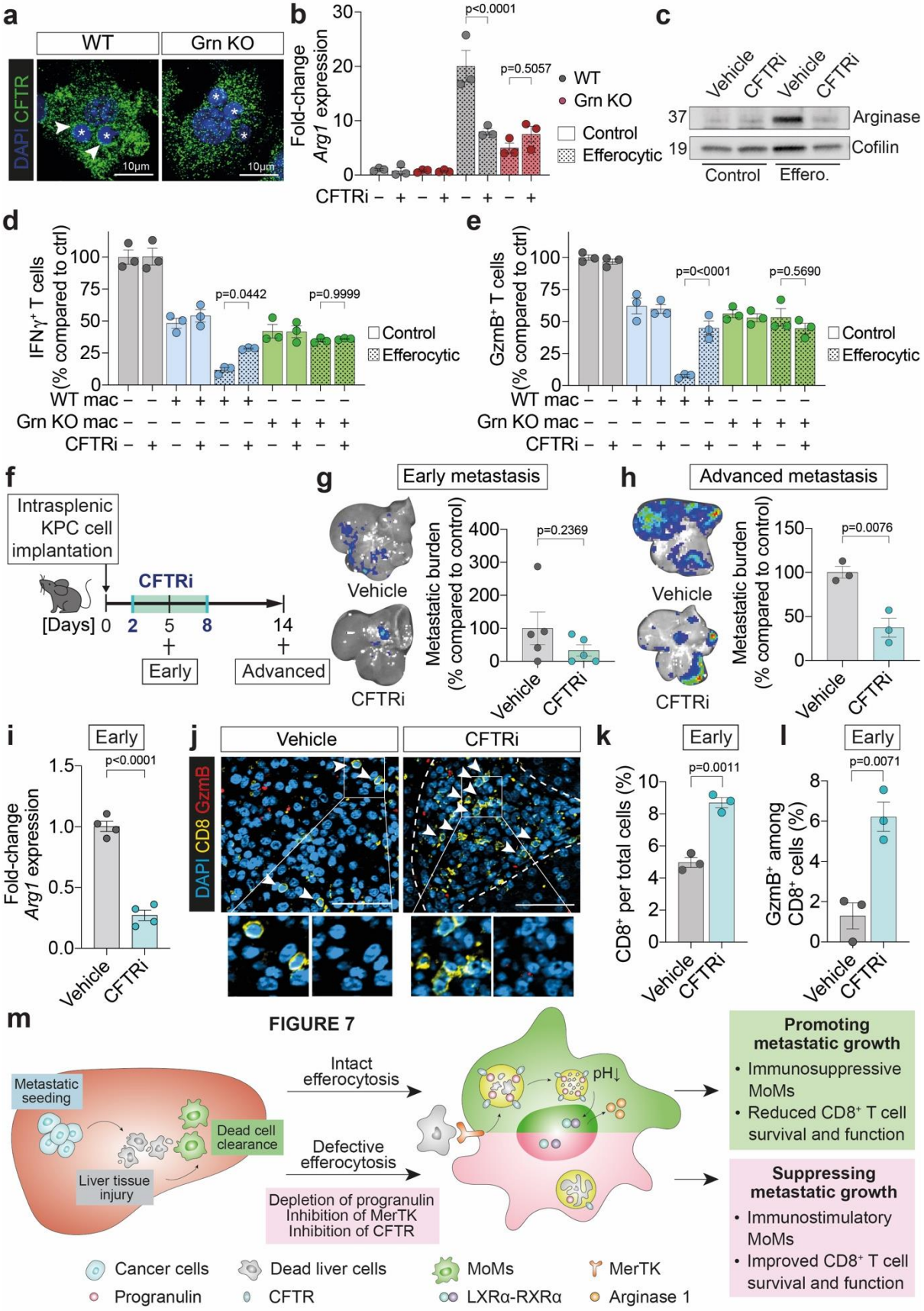
a
WT
Grn KO
DAPI CFTR
10μm
b
Fold-change Arg1 expression
p<0.0001
p=0.5057
WT
Grn KO
Control
Efferocytic
CFTRi
c
Vehicle
CFTRi
Vehicle
CFTRi
37
Arginase
19
Cofilin
Control
Effero.
d
IFNγ+ T cells (% compared to ctrl)
p=0.0442
p=0.9999
Control
Efferocytic
WT mac
Grn KO mac
CFTRi
e
GzmB+ T cells (% compared to ctrl)
p=0<0001
p=0.5690
Control
Efferocytic
WT mac
Grn KO mac
CFTRi
f
Intrasplenic KPC cell implantation
CFTRi
[Days] 0 2 5 8 14
Early
Advanced
g
Early metastasis
Vehicle
CFTRi
Metastatic burden (% compared to control)
p=0.2369
Vehicle
CFTRi
h
Advanced metastasis
Vehicle
CFTRi
Metastatic burden (% compared to control)
p=0.0076
Vehicle
CFTRi
i
Early
Fold-change Arg1 expression
p<0.0001
Vehicle
CFTRi
j
Vehicle
CFTRi
DAPI CD8 GzmB
k
Early
CD8+ per total cells (%)
p=0.0011
Vehicle
CFTRi
l
Early
GzmB+ among CD8+ cells (%)
p=0.0071
Vehicle
CFTRi
m
FIGURE 7
Metastatic seeding
Liver tissue injury
Dead cell clearance
Intact efferocytosis
Defective efferocytosis
Depletion of progranulin
Inhibition of MerTK
Inhibition of CFTR
pH↓
Promoting metastatic growth
• Immunosuppressive MoMs
• Reduced CD8+ T cell survival and function
Suppressing metastatic growth
• Immunostimulatory MoMs
• Improved CD8+ T cell survival and function
Cancer cells
Dead liver cells
MoMs
MerTK
Progranulin
CFTR
LXRα-RXRα
Arginase 1

Figure 7. Inhibition of progranulin-regulated CFTR impairs efferocytosis-induced macrophage polarisation

(a) Representative immunofluorescence images of CFTR in WT or Grn KO BMM following 2-hour incubation with apoptotic thymocytes (experiment was performed twice with similar results). Asterisks indicate engulfed apoptotic cells.

(b) Fold expression of *Arg1* as assessed by qPCR in WT or Grn KO BMMs following 20-hour incubation with apoptotic thymocytes (ApopT) with control or CFTRi treatment (n=3 biological replicates/group). Data are presented as mean ± SEM. Statistical analysis was performed using two-way ANOVA with Sidak's post-test.

(c) Representative Western blot image of arginase 1 and loading control cofilin levels in control and efferocytic WT or Grn KO BMMs following 3-hour co-culture with apoptotic thymocytes and further 17-hour incubation with or without CFTRi treatment (experiment was performed three times with similar results).

(d-e) Relative $CD8^+$ T cell activation measure by percentages of $IFN\gamma^+$ **(d)** or granzyme B $(GzmB)^+$ **(e)** $CD8^+$ T-cells following stimulation with anti-CD3/CD28-coupled Dynabeads and co-culture with efferocytic WT or Grn KO BMMs (post 4-hour incubation with apoptotic thymocytes) with or without CFTRi treatment compared to Dynabeads-only control (n=3 biological replicates/group). Data are presented as mean ± SEM. Statistical analysis was performed using one-way ANOVA with Sidak's post-test.

(f-l) Liver metastasis was induced by intrasplenic implantation of $KPCLuc^{/ZsGreen}$ cells. Intraperitoneal administration of 0.5mg/kg CFTRinh172 (CFTRi) or vehicle control (vehicle) was given daily from day 2 to 8 post implantation. Early (d5) and advanced (d14) metastatic livers were resected and analysed.

(f) Schematic diagram illustrating the CFTRi experiment timeline.

(g) Representative *ex vivo* bioluminescence imaging (BLI) images (left) and relative total flux (% tumour burden, right) of early metastatic livers (d5) from CFTRi-treated compared to vehicle control-treated mice (n=5 mice/group). Data are presented as mean ± SEM. Statistical analysis was performed using unpaired t-test.

(h) Representative *ex vivo* bioluminescence imaging (BLI) images (left) and relative total flux (% tumour burden, right) of advanced metastatic livers (d14, endpoint) from CFTRi-treated compared to vehicle control-treated mice (n=3 mice/group). Data are presented as mean ± SEM. Statistical analysis was performed using unpaired t-test.

(i) Fold expression of *Arg1* early MoMs ($F4/80^+TIM4^-$) from mice treated with CFTRinh172 (CFTRi) compared to vehicle control as assessed by qPCR (n=4 mice/group). Data are presented as mean ± SEM. Statistical analysis was performed using unpaired t-test.

(j, k) Representative immunofluorescence images (**j**) and quantificationof intralesional $CD8^+$ T-cells (**k**) and proportion of cytotoxic $GzmB^+$ T cells **(l)** in early metastasis from mice treated

with vehicle or CFTRinh172 (CFTRi). Arrowheads indicate $CD8^+$ T cell (green), nuclei were counterstained with DAPI (blue) (n=3 mice/group). Scale bars 50 µm. Data are presented as mean ± SEM. Statistical analysis was performed using unpaired t-test.

(m) Graphical schematic summarising the role of efferocytic macrophages in PDAC liver metastasis. During early stage of metastasis, seeding of cancer cells induces liver injury leading to clearance of dead cell debris by monocyte-derived macrophages (MoMs) via receptor MerTK. Engulfed dead cells are degraded in acidic phagolysosome lumen, a process that is dependent on lysosomal acidification by progranulin (PGRN) and CFTR. Following efficient lysosomal degradation of the dead cell cargo, LXRα is activated and induces expression of the T cell inhibitory factor, arginase 1. Arginase 1-mediated reduction in T cell numbers and activation eventually facilitates metastatic outgrowth. Impairment in these processes and suppression of tumour growth can be achieved via depletion of progranulin or blockade of MerTK or CFTR functions.